Cross-scale visualization of RNA dynamics in whole plants using an RNA-triggered reporting system

Jiuyuan Bai[1, 2, †], Yazhou Chen[3, 4, †], Jiayu Zhang[1], Hongpei Ren[1], Shan Pan[1], Yiran Tao[1], Miaomiao Lei[1], Mengyue Dong[1], Sha Liu[1], Jia Yi[1], Fang Chen[1], Jiang Li[5, *], Chunhai Fan[6, *], Yun Zhao[1*]

[1]Key Laboratory of Bio-Resource and Eco-Environment of Ministry of Education, College of Life Sciences, Sichuan University, Chengdu 610065, China.

[2]Microbiology and Metabolic Engineering Key Laboratory of Sichuan Province, College of Life Sciences, Sichuan University, Chengdu 610065, China.

[3]Hubei Hongshan Laboratory, Wuhan 430070, China.

[4]Hubei Insect Resources Utilization and Sustainable Pest Management Key Laboratory, College of Plant Science and Technology, Huazhong Agricultural University, Wuhan 430070, China.

[5]Institute of Materiobiology, College of Sciences, Shanghai University, Shanghai 200444, China.

[6]Institute of Translational Medicine, Shanghai Jiao Tong University, Shanghai 200240, China.

†J.B. and Y.C. contributed equally to this work.

*Corresponding author. Email: zhaoyun@scu.edu.cn； fanchunhai@sjtu.edu.cn; lijiang80@shu.edu.cn

Abstract

Real-time visualization of RNA dynamics across spatial scales in living plants is desirable yet remains challenging, hindered by the absence of imaging tools that simultaneously offer high sensitivity and deployability in whole living plants. Here, we engineered a modular, RNA-triggered fluorescence (RTF) reporter system *de novo* for spatiotemporal imaging of RNA from cellular to whole-plant scales *in vivo*. This system integrates three functional modules: a target-specific allosteric RNA switch, a degradable adapter for background suppression, and a fluorescent reporter. All components are stably expressed from a single vector and assemble *in vivo*, enabling uniform deployment throughout entire plants. The modified RTF (RTFst) achieves single-molecule sensitivity (signal-to-noise ratio >60) for dynamic tracking of developmentally regulated, tissue-specific, circadian, and stress-responsive mRNAs. Crucially, it enables the first direct, real-time observation of graft-transmissible mRNA trafficking across tissue scales and cross-kingdom transfer of the aphid-secreted long non-coding RNA *Ya1* to plant cells. RTF establishes a versatile platform for studying gene regulation, signaling, and transcript mobility in plants, with broad applicability in synthetic biology and crop improvement.

Introduction

RNA accumulation is highly dynamic and deeply intertwined with the physiological state of the whole organism [1-3], however, capturing these dynamics at the scale of whole living systems remains a significant challenge in biology.

Whole living organisms are important for understanding RNA expression dynamics [4], which reflect the complex regulatory networks governing growth, development, and adaptation to environmental changes. Within individual cells, RNA expression is shaped not only by the local cellular conditions but also by systemic signals originating from distant tissues [5-9]. These processes are further modulated by external environmental signals that directly act on the organism as a whole. Moreover, RNAs are often trafficked between tissues, underscoring their dynamic nature and functional importance [5]. Intriguingly, living organisms frequently acquire RNAs from other organisms that belong to entirely different biological kingdoms, with transfer of insect RNAs known to occur into plants on which the insect feeds [10-13]. Those RNAs function within the recipients, mediating intimate interspecies relationships [14]. Profiling such RNA dynamics across

53 time and space at the scale of whole living organisms is crucial for understanding gene regulation
54 and ecological interactions within interconnected physiological and environmental contexts.
55 However, achieving this is difficult, in particular for biotic interactions.

56 Over the past few decades, numerous single-molecule RNA tracking techniques have been
57 developed to visualize RNA dynamics in living systems, largely in animal systems. These
58 approaches generally fall into two major categories. The first relies on genetically encoded tags
59 appended to target RNAs, such as fluorescent RNA aptamers[15, 16] or RNA motifs such as MS2 that
60 recruit exogenous reporters (e.g., fluorescent proteins) [1]. While these systems have enabled high-
61 resolution imaging, the introduction of RNA tags can perturb the native properties of the RNA,
62 including its abundance, expression dynamics, stability, subcellular localization, and mobility [17-
63 20]. A second category comprises methods that detect endogenous RNAs via trans-binding probes,
64 either chemically synthesized or genetically encoded. This group includes molecular beacons[21],
65 split probes[22] and CRISPR-based reporters[23-26]. Although these methods, in principle, detect
66 unmodified RNAs, they are often limited by high background fluorescence, insufficient spatial
67 resolution for single-molecule level, and inefficient or non-uniform probe distribution across large,
68 complex live tissues[27]. Recently, a split ribozyme system was adapted for *in vivo* RNA imaging in
69 plants [28]. While promising, its reliance on ribozyme-mediated GFP transcript reassembly followed
70 by translation introduces a temporal lag incompatible with real-time RNA tracking. Moreover,
71 ribozyme splicing efficiency is highly variable in plant cells due to the complex intracellular
72 environment, further limiting its applicability for visualizing long-distance RNA trafficking at
73 single-molecule resolution *in vivo*.

74 To address these limitations, we developed an RNA switch-controlled RNA-triggered
75 fluorescence system (RNA switch–RTF), enabling high-resolution and sensitive visualization,
76 monitoring, and quantification of RNA dynamics in living plants. Using RNA switch–RTF, we
77 tracked *in vivo* expression dynamics of multiple conditionally expressed RNAs in the model plant
78 *Arabidopsis thaliana* at subcellular and single-cell resolution throughout the entire plant. RNA
79 switch–RTF demonstrated cell-to-cell trafficking of *TRANSLATIONALLY CONTROLLED*
80 *TUMOR PROTEIN 1* (*TCTP1*) mRNAs [29] in *A. thaliana* and systematic migration of aphid-derived
81 long non-coding RNA *Ya1* [30] in its leaves. This approach provides a robust tool for studying RNA
82 localization and movement *in vivo*, offering critical insights into RNA function in plant
83 development and physiology, and ecological interactions.

Results

De novo design of an RNA-triggered fluorescence (RTF) reporter system

We sought to develop a fluorescent reporter system to visualize specific RNA molecules in whole plants. In this system, GFP fluorescence would be detectable only when the target RNA is present. This requires GFP to be constitutively degraded in plants in the absence of the target RNA, with degradation inhibited upon the presence of the target (Fig. 1A). Theoretically, constitutive GFP degradation can be achieved by tagging it with degron sequences[31]— minimal motifs that recruit 26S proteasomes to target proteins.

Although several degrons have been characterized in plants [32, 33], their relatively large size limits their suitability for adaptation into compact RNA-binding peptides. Therefore, we first identified degrons in leaves of the model plant *Nicotiana benthamiana* that is amenable to and convenient for transient and stable transformation. By comparative proteomics, 17 proteins strongly accumulated only in leaves treated with the proteasome inhibitor MG132, compared to mock-treated controls (Table S1, Fig. S1A–C). We fused 20 amino acids at the C-terminus of these 17 proteins to the C-terminus of GFP and tested their ability to promote GFP degradation relative to an mCherry internal control (Fig. S1D, E). Twenty residues at the C terminus of Niben261Chr01g0008021.1 (encoding a predicted subtilisin-like protease SBT6) enhanced GFP degradation (Fig. 1B, Fig. S1E). Further analysis identified the final four residues of this protein, RRRG, as a degron capable of efficiently promoting GFP degradation (Fig. 1B, Fig. S1F).

To enable GFP degradation precisely in response to the target RNA, we chose six well-characterized RNA-binding peptides (RBP) [34-39] (Table S2), each with specificity for RNA cognate aptamer. Fusion of the RRRG degron to the C terminal of these RBPs did not affect their capacity to bind RNA (Fig. 1C, Fig. S1G). To assess the functionality of these RBPs fused with RRRG, we next tested the abundance of GFP tagged with RBP–RRRG in the presence and absence of specific RNA aptamers. Of these, GFP–BTat–RRRG and GFP–Rev–RRRG accumulated in *N. benthamiana* leaves when exposed to RNA aptamers Pepper and RRE, respectively (Fig. 1D, Fig. S1H). GFP–Rev–RRRG showed superior performance, with strong GFP fluorescence in the presence of RRE, while no signal was detectable in its absence by fluorescence imaging (Fig. 1E) and western blotting (Fig. S1, H and I).

114 In sum, we successfully developed RNA-triggered fluorescence (RTF) by manipulating GFP
115 degradation to visualize the presence of an RNA ligand in plants.

116 **Engineering of RNA switches to control GFP degradation for use with RTF**

117 The RNA aptamer RRE binds to Rev and inhibits the recruitment of the proteasomes to the degron
118 on the GFP–Rev–RRRG chimeric protein (Fig. 1D, E). Building on this, we engineered RNA
119 switches capable of controlling GFP degradation in the presence of specific target RNA molecules.
120 To achieve this, we constructed RNA switches based on RRE (39 nt) that incorporate three
121 functional elements: a probe sequence complementary to the target RNA and two linker sequences
122 that hybridize with the RRE and the probe, respectively (Fig. 1F).

123 Theoretically, in the absence of the target RNA, the RNA switch adopts an inactive
124 conformation whereby the linkers hybridize with the RRE and the probe. This folding prevents the
125 RRE from binding to the degron, leading to GFP degradation (Fig. 1G). Conversely, when the
126 target RNA is present, the RNA switch transitions to an active conformation through base pairing
127 between the probe and the target. This conformational change allows RRE to bind to the degron,
128 leading to GFP accumulation (Fig. 1G).

129 To evaluate the functionality of the RNA switch, we designed various combinations of probes
130 and linker sequences, and tested their ability to regulate GFP levels in the presence and absence of
131 the target RNA. Using a stable-transgenic *N. benthamiana* line expressing *mCherry* under the 35S
132 promoter, we designed 12 distinct probes to target different regions of *mCherry* mRNA (Fig. S2A,
133 Table S3). The RNA switch plasmid and the GFP–Rev–RRRG plasmid in *Agrobacterium*
134 *tumefaciens* were co-infiltrated into *N. benthamiana* leaves of both *mCherry* and wild-type (WT)
135 backgrounds. Probes 2 and 8 demonstrated functionality (Fig. S2, B and C). In WT plants, these
136 probes maintained the RNA switch in an inactive state, as evidenced by the absence of detectable
137 GFP fluorescence (Fig. 1H). In *mCherry* plants, however, these probes enabled the RNA switch
138 to bind the degron, resulting in strong GFP fluorescence (Fig. 1H).

139 RNA switches with probes 2 and 8 adopted a dumbbell-shaped structure (Fig. S2A), which
140 appears critical for functionality. The switch incorporated with probe 2 has a shorter stem sequence
141 and a larger bottom loop, enhancing its efficiency. Other structural configurations failed to regulate
142 GFP signals effectively (Fig. S2, A to C), underscoring the importance of the dumbbell-shaped
143 conformation for RNA switch performance.

144 These engineered RNA switches effectively control the RTF system and enable precise
145 regulation of GFP degradation in response to specific RNA molecules.

146 **Optimization of the RNA switch-controlled RTF system in plants**

147 To evaluate the RNA switch–RTF system in plants, we constructed a plasmid containing an RNA
148 switch targeting the Arabidopsis *CHORISMATE MUTASE 3* (*CM3*) mRNA driven by the *U6*
149 promoter, and GFP–Rev–RRRG under the control of the *UBQ10* promoter (Fig. 2A). These
150 expression modules were introduced into both Arabidopsis wild-type (WT) and *cm3* mutant plants
151 (Fig. 2A). In WT plants, strong GFP signals were observed, but *cm3* mutant plants also produced
152 weak but detectable GFP signals (Fig. 2B), indicating that the system displayed some degree of
153 signal leakage. The leakage was also confirmed by the observation of GFP in WT plants expressing
154 RNA switch–RTF that were treated with the RNA synthesis inhibitor Actinomycin D (Fig. S3, A
155 and B).

156 To address this issue, we incorporated two additional strategies: a split fluorescent protein
157 (SFP) approach [3] and SunTag [40] (Fig. 2C). In the SFP strategy, GFP–Rev–RRRG was replaced
158 with two modules: $GFP_{1–10}$ and 24×GFP_{11}–Rev. With SunTag, GFP–Rev–RRRG was also
159 replaced with two components: full-length *GFP* fused to a single-chain antibody (scFv) tagged
160 with the RRRG degron and 24×GCN4 tagged with Rev at its N-terminus. These systems,
161 combined with RNA switches targeting *CM3* mRNA, were introduced into WT and *cm3* mutant
162 plants. RTF–SunTag plants expressed an extremely low GFP signal in *cm3* mutant plants
163 compared to the RTF, RTF–SFP systems (Fig. 2, D and E, Fig. S3C), likely due to degradation of
164 unbound GFP.

165 We also compared the RTF–SunTag with dCas13–SunTag system, a robust RNA imaging
166 tool in mammalian cells. However, in *cm3* mutant, dCas13–SunTag system produced high
167 background fluorescence, resulting in false positives and difficult to interpret the signal in WT
168 plants (Fig. 2, D and E). This background is likely due to large vacuoles in plant cells, which
169 compress the cytosol in a thin peripheral layer, concentrating even minor cytosolic fluorescence
170 and thereby amplifying background noise[41]. In contrast, the RTF–SunTag system mitigated this
171 issue by incorporating a degron we screened (Fig. 2C), which significantly reduced background
172 and yielded a 12-fold increase in signal-to-background (S/B) ratio compared to the dCas13–
173 SunTag system (Fig. 2, D and E).

174 To assess the accuracy of the RNA switch–RTF–SunTag system, we compared the
175 localization of *CM3* mRNA indicated by RTF–SunTag with that determined by smFISH using a
176 series of Cy3-labeled probes targeting *CM3* mRNA. Colocalization of GFP and Cy3 signals was
177 observed in the leaves and roots of transgenic Arabidopsis plants containing RNA switch–RTF–
178 SunTag (Fig. 2, F to G, Fig. S3, E and F), confirming its accuracy in detecting *CM3* mRNA
179 localization.

180 In summary, the RNA switch–RTF system, optimized with SunTag and hereafter referred to
181 as RNA switch–RTFst, accurately localizes the target RNA within plant cells, providing a robust
182 and reliable tool for studying RNA dynamics and their subcellular localization.

183

184 **RNA subcellular localization is unaffected by RNA switch–RTFst**

185 RNA function is often closely tied to subcellular localization [42]. We designed three
186 experiments to assess whether RNA switch–RTFst influences RNA localization. First, we
187 compared *CM3* subcellular localization resulting from the RNA switch–RTFst system with those
188 from the mCherry–MCP–MS2 system. In the latter system, repeated *MS2* sequences were fused to
189 the 3' UTR of *CM3* mRNA, allowing the MS loops on the hybrid RNA to capture MCP from the
190 mCherry–MCP protein (Fig. 3A). *CM3* mRNAs localized in both nuclei and the cytoplasm (Fig.
191 3A). With RNA switch–RTFst, probe sequences targeting the 5' UTR, coding sequence, and 3'
192 UTR of *CM3* were designed (Table S5). Probes targeting the coding sequence showed identical
193 subcellular localization patterns to those observed with the mCherry–MCP–MS2 system (Fig. 3A,
194 Fig. S3, G and H). Probes targeting the 5' UTR should be used with caution because these tend to
195 detect fewer RNA molecules per cell.

196 Second, the RNA switch-controlled RTFst system with a probe targeting *CM3*, and *CM3–*
197 *6×MS2* RNA was co-expressed in protoplast cells obtained from *N. benthamiana* leaves. GFP
198 signals revealed that *CM3–6×MS2* RNA was predominantly localized in the cytoplasm and was
199 nearly undetectable at the plasma membrane (Fig. 3, B and C). However, when MCP tagged with
200 CAAX (a membrane-targeting motif) [43] was introduced, GFP signal along the membrane increased
201 (Fig. 3, B and C). This change was attributed to the binding of MS loops on *CM3–6×MS2* RNA
202 to MCPs at the membrane. These results suggest that the localization of *CM3–6×MS2* RNA, even
203 when complexed with the RNA switch–RTFst, remained unaffected.

204 Third, we evaluated the RNA switch–RTFst system using the mitochondria-localized RNA
205 *VDAC3* (*VOLTAGE-DEPENDENT ANION CHANNEL 3*), which has been reported to reside in
206 the mitochondria of *N. benthamiana* cells [44]. RNA switch–RTFst and *VDAC3* RNA were co-
207 expressed in *N. benthamiana* leaves. Over time, the GFP signal became increasingly proximal to
208 mitochondria (Fig. 3, D and E). This progressive colocalization suggested that *VDAC3* RNA was
209 unaffected by the system and remained associated with its expected subcellular compartment, the
210 mitochondria.

211 RNA switch–RTFst does not detectably alter the subcellular localization of RNA in plants,
212 maintaining native localization patterns of at least these target transcripts.

213

214 **RNA switch–RTFst is suitable for real-time monitoring of RNA dynamics in living plants**

215 To enable real-time monitoring of RNA dynamics in living plants, we applied the RNA
216 switch–RTFst to a set of transcripts representing diverse regulatory contexts. Specifically, we
217 selected *TUB5* (*TUBULIN β-5*) for development-dependent expression [45], *SMB* (*SOMBRERO*) for
218 tissue-specific expression [46], *CCA1* (*CIRCADIAN-CLOCK-ASSOCIATED 1*) for circadian
219 regulation [47], and *CIPK11* (*CBL-INTERACTING PROTEIN KINASE 11*) for stress responsiveness,
220 particularly to cadmium (Cd) [48] (Table S6). RNA switches targeting the coding sequences of those
221 RNAs were introduced, along with RTFst, into *A. thaliana* wild-type plants.

222 *TUB5* mRNA is ubiquitously expressed in *A. thaliana*, with lower levels in vegetative tissues
223 and higher levels in stems and reproductive tissues. GFP signals were detected across all examined
224 tissues (Fig. 4, A and B). During development, signals remained relatively stable in roots but
225 became stronger in flowers (Fig. 4, A and B, Fig. S4, A and B). RNA switch–RTFst showed no
226 obvious effect on the expression, turnover, or translation of *TUB5* mRNA, or on overall
227 ubiquitination patterns (Fig. S5 A to E).

228 *SMB* was exclusively expressed in the specialized zones of roots, mainly in the elongation
229 zone of roots in 3- and 5-d-old seedlings, with a gradual increase in expression observed in the
230 maturation zone of 7-d-old seedlings (Fig. 4C, Fig. S4, C and D). *CCA1* is a circadian-regulated
231 RNA that exhibits time-of-day-specific expression [47]. Consistent with this, here its abundance
232 displayed dynamic changes during the morning and evening phases (Fig. 4D, Fig. S4, E to F).

233 *CIPK11*, a Cd-responsive mRNA [48], was up-regulated in roots 12 h after Cd treatment, followed
234 by gradual down-regulation at 18 h (Fig. 4D, Fig. S4, H to I). These dynamic expression patterns
235 identified by RNA switch–RTFst were validated by qRT–PCR (Fig. 4, E and F, Fig. S4, G and J).

236 Altogether, RNA switch–RTFst is a powerful tool to visualize and monitor the *in vivo*
237 dynamics of RNA expression in living plants, offering insights into development, tissue specificity,
238 circadian regulation, and stress responses.

239

240 **RNA switch–RTFst monitors** the **movement of mobile RNAs in living plants**

241 In plants, transcripts can move to distant tissues, potentially acting as systemic signals
242 regulating development and growth [49]. *TCTP1* mRNA has long-distance mobility, traveling from
243 the shoot to the root through the phloem [29]. To track this movement, we expressed the *TCTP1*-
244 targeted RNA switch–RTFst system in *tctp1* mutants (*tctp1–RTFst*) (Fig. 5A). Grafting
245 experiments were then conducted using wild-type shoots as the scion and *tctp1–RTFst* roots as
246 stock (Fig. 5A). At 72 h post-grafting, GFP signals progressively intensified, particularly at 5 mm
247 below the graft junction (Fig. 5, B and C), and stronger GFP signals accumulated in root sections
248 further from the junction over time (Fig. 5, B and C). Time-lapse imaging confirmed the movement
249 of *TCTP1* mRNA across the graft junction (Fig. 5, B and D, Movie 1). Upon reaching the root,
250 *TCTP1* mRNA is known to influence lateral-root formation and regulate root architecture (*32*).
251 Root length in grafted plants was comparable to that of WT and statistically significantly longer
252 than in *tctp1* mutants (Fig. 5D), suggesting that WT-derived *TCTP1* mRNA compensated for the
253 loss of function in the roots. This compensation was unaffected by RNA switch–RTFst expression
254 in the roots.

255

256 **RNA switch–RTFst can visualize the aphid-secreted lncRNA *Ya1* in plants**

257 Beyond endogenous RNA movement within plants, RNAs can also be transferred between
258 organisms from distinct biological backgrounds [50], with the green peach aphid *Myzus persicae*
259 translocating the lncRNA *Ya1* into host plants via feeding [30]. To investigate the mobility of this
260 aphid-secreted RNA, we designed a *Ya1*-targeted RNA switch–RTFst and transiently expressed it
261 in *N. benthamiana* leaves. When co-expressed with *Ya1*, GFP signals were detected in the

262 cytoplasm and nuclei of infiltrated cells (Fig. 6A). In leaves where the construct was expressed
263 and subsequently fed on by aphids, GFP signals accumulated at the feeding sites (Fig. 6A).
264 Furthermore, when the system was expressed in two separate infiltration sites on the same leaf,
265 with one co-expressing *Ya1*, GFP signals were observed at the distal site, even in the absence of
266 direct *Ya1* expression (Fig. 6B, Movie 2). To visualize the dynamics of *Ya1* translocation, *N.*
267 *benthamiana* leaves expressing *Ya1*-targeted RNA switch–RTFst were exposed to aphid feeding
268 and monitored by time-lapse imaging. After 6 h of continuous feeding, GFP signal was detectable
269 and intensified over time, while control leaves expressing RNA switch–RTFst but without aphid
270 feeding exhibited no detectable GFP signal (Fig. 6C).

271 These findings confirm the mobility of an aphid-secreted cross-kingdom RNA into the host
272 plant.

273 **Discussion**

274 Monitoring RNA expression dynamics in living systems at the whole-organism scale remains
275 a fundamental challenge in biology. Here, we have addressed this issue by introducing RNA
276 switch–RTF, a *de novo* designed tool for visualizing RNA expression dynamics in living plants.
277 RNA switch–RTF enables high-sensitivity detection of target RNAs while preserving their native
278 localization and function.

279 Live-cell RNA-imaging technologies have become indispensable for quantitatively analyzing
280 expression dynamics[51]. However, such methods have limitations that hinder monitoring of real-
281 time RNA dynamics at the whole-organism scale. Nucleic acid molecular beacons [21] and
282 nanoparticle-based nano-flares [52] produce fluorescence upon structural reconfiguration triggered
283 by RNA binding. However, efficient delivery of these exogenously synthesized probes into plant
284 cells remains a major challenge due to the barrier of cell walls [3]. Fluorescent RNA aptamers and
285 RNA motifs that recruit RNA-binding fluorescent proteins offer another strategy for RNA
286 visualization [53-55], but require tissue separation, which disrupts native RNA expression patterns
287 and compromises spatial regulatory information. CRISPR–dCas-based imaging enables
288 visualization of diverse RNAs and their subcellular localization [56], yet its application in plant cells
289 is confounded by cytosolic fluorescence artifacts [41]. A split-ribozyme system was introduced as an
290 alternative for *in vivo* RNA imaging in plants [28]. This approach disrupts sfGFP translation by
291 incorporating a self-splicing ribozyme into its coding sequence, allowing translation to proceed

292 only after the ribozyme excises and transcript ligation. While promising when target RNA and
293 sfGFP translation occur in the same cell, the temporal delay between transcript rejoining and
294 protein synthesis constrains its utility for real-time RNA tracking.

295 The effectiveness of RNA switch–RTF relies on RNA-triggered fluorescence (RTF) and
296 programmable RNA switches. A critical component of RTF is the degron RRRG, which drives
297 continuous GFP degradation. While several degrons have been identified in plants, including the
298 Auxin-inducible degron (AID) [33] and mini-Auxin inducible degron (mIAA) [32], their lengths,
299 ranging from 67–110 amino acids for AID and 40–50 amino acids for mIAA, render them
300 unsuitable for development into RNA-binding peptides. To overcome this limitation, we
301 conducted a proteome-wide screening of constitutively degraded proteins in plants, leading to the
302 identification of RRRG, a 4-amino-acid degron located at the C-terminus of
303 Niben261Chr17g0072018. This represents the smallest known degron identified in plants to date.
304 RRRG did not disrupt the RNA-binding activity of select RBPs or their interaction with specific
305 RNA ligands.

306 The second key component of RNA switch–RTF is the RNA switch itself, which regulates
307 the degradation of GFP-RRRG. Exploiting the high affinity between Rev–RRRG and the RNA
308 aptamer RRE [38], we engineered RNA switches by incorporating probe and linker sequences into
309 RRE. Systematic testing of probe–linker combinations led to the identification of dumbbell-shaped
310 RNA switches capable of modulating GFP degradation in response to specific RNAs. This
311 regulation is mediated by RNA allostery, wherein binding to target RNAs induces conformational
312 changes that alter the ability of RRE to interact with the degron on GFP-RRRG. These RNA
313 switches represent the first known successfully engineered RNA-based regulatory elements in
314 plants, demonstrating robust functionality across transient expression systems, including
315 protoplasts and agroinfiltrated leaves, as well as in stable-transgenic lines.

316 Integration of the RNA switch–RTF system with SunTag [40] markedly enhances the sensitivity
317 and precision of RNA detection by degrading free GFP. Crucially, the RNA switch–RTFst
318 complex does not perturb the localization, expression, turnover, or translation of target RNA
319 molecules. It also preserves target RNA function, as demonstrated by the successful compensation
320 of shoot-derived *TCTP1* mRNA in the root tissues of *tctp1* mutants expressing the RNA switch–
321 RTFst complex. Beyond its utility in tracking RNA dynamics in living plants, RNA switch–RTF

322 holds promise in RNA-triggered immune responses. By engineering the system to detect pest-
323 secreted RNAs [10, 11], it could be repurposed to trigger the accumulation of pest-specific defense
324 molecules instead of GFP. Similarly, many plant pathogens secrete RNAs into host cells even at
325 early infection stages [50, 57, 58]. RNA switch–RTF can be designed to recognize pathogen-derived
326 RNAs and activate species-specific immune responses. However, the system has several
327 limitations. The RNA switch requires a stable dumbbell-shaped structure, constraining its
328 compatibility to transcripts with suitable sequences. Additionally, the ~21-nt probe in the RNA
329 switch may exhibit off-target effects. Probe accessibility depends on maintaining an unpaired
330 configuration, which can be disrupted by intracellular or extracellular factors that alter RNA
331 structure, compromising target recognition and overall switch performance.

332 These findings establish RNA switch–RTF as a versatile platform for RNA imaging and
333 functional studies while opening new and sustainable avenues for enhancing plant immunity
334 against pests and pathogens.

335 **Materials and Methods**

336 Plant materials and growth conditions

337 Seeds of *Nicotiana benthamiana* and *A. thaliana* Columbia (Col-0) were surface-sterilized
338 and germinated on 1× Murashige and Skoog (MS) medium with 1% [w/v] Sucrose. For normal
339 growth conditions, plants were grown at 23°C under long-day conditions (LD, 16-h light /8-h dark
340 cycle) with a light intensity of 150 μmol m^{-2} s^{-1} in a plant growth chamber.

341 The *A. thaliana* mutants *cm3* (SALK_011276.36.40.x) *and tctp1* (CS486456, heterozygous)
342 were obtained from the Arabidopsis Biological Resource Center (ABRC). Homozygous plants
343 were used and primers for genotyping are listed in Table S7.

344 For tobacco *mCherry* lines, we introduced *35S::mChery* construct into *Nicotiana*
345 *benthamiana* by Agrobacterium tumefaciens-mediated transformation. The overexpression lines
346 were confirmed by quantitative real-time PCR（qRT-PCR）.

347 Agroinfiltration of *N. benthamiana*

348 *Agrobacterium tumefaciens* GV3101 stocks were streaked on LB plates supplemented with
349 kanamycin (50 μg/mL) and rifampicin (25 μg/mL). After overnight culture in liquid LB, cells were
350 pelleted, resuspended in infiltration medium (10 mM MES, pH 5.6; 10 mM $MgCl_2$; 150 μM

351 acetosyringone), and adjusted to an OD_{600nm} of ~0.6. After a 2-h incubation, the suspension was
352 infiltrated into the abaxial side of 3-week-old *N. benthamiana* leaves using a needleless syringe.
353 Co-infiltration used a 1:1 volume ratio of bacterial solutions containing constructs of interest.
354 Plants were maintained in growth chambers (LD; 16-h light /8-h dark cycle, with a light intensity
355 of 150 μmol m^{-2} s^{-1}) for 3 d before leaf samples were collected for confocal microscopy.

356 Identification of putative degrons in *N. benthamiana*

357 Leaves of 6-week-old *N. benthamiana* were treated with either 10 μM MG132 or mock
358 solution (1× PBS buffer) for 24 h, respectively. Following the treatment, leaves were harvested for
359 LC–MS/MS at Shanghai Personalbio Technology Company. Proteins were extracted using
360 TCA/acetone precipitation and the SDT (4% SDS, 100 mM DTT, 150 mM Tris-HCl pH 8.0) lysis
361 method[59]. The mixture was sonicated, boiled, and centrifuged to separate the supernatant. Protein
362 concentration was determined using the BCA Protein Assay Kit (Cat. A65453, Thermo Scientific),
363 and 15 μg of protein from each sample was mixed with 5× SDS loading buffer and boiled. The
364 proteins were separated on a 4–20% SDS–PAGE gel and visualized with Coomassie Blue R-250
365 staining. Protein digestion was performed by adding DTT (40 mM) to each sample, mixing at 600
366 rpm for 1.5 h (37°C), and then adding IAA (20 mM) to block reduced cysteine residues. The
367 samples were then transferred to filters (Microcon units, 10 kDa), washed with UA buffer (8 M
368 urea, 100 mM Tris-HCl pH 8.0) and 25 NH_4HCO_3 buffer, then trypsin was added (trypsin:protein
369 (w/w) ratio was 1:50) and incubated at 37°C for 15–18 h. The resulting peptides were collected,
370 desalted on C18 Cartridges (Cat.66871-U, Sigma), concentrated by vacuum centrifugation, and
371 reconstituted in 0.1% v/v formic acid.

372 For the analysis of data-independent acquisition (DIA) experiments, iRT (indexed retention
373 time) calibration peptides were spiked into the sample and analyzed by an OrbitrapTM AstralTM
374 mass spectrometer connected to a Vanquish Neo system liquid chromatography in DIA mode. The
375 precursor ions were scanned at a mass range of 380–980m/z, and the MS1 resolution was 240,000
376 at 200 m/z. DIA data were analyzed with DIA-NN software [60], and protein identification was based
377 on 99% confidence and a false-discovery rate ≤ 1%. Proteins were identified by searching MS/MS
378 against the InterPro member database Pfam.

379 To evaluate the degradation efficiency of putative degron sequences, the 60 nucleotides
380 (corresponding to 20 amino acids) for each gene were fused to the C terminus of the GFP sequence

381 in a 2A self-cleaving peptide co-expression plasmid (Table S1). This plasmid also co-expresses
382 mCherry alongside GFP. Various truncated versions of CP-12 (Niben261Chr17g0072018) were
383 generated and inserted into the plasmid. These plasmids were introduced to *N. benthamiana* leaves
384 via agroinfiltration. Degradation efficiency was assessed by comparing GFP signal intensity to
385 that of mCherry. Fluorescence images were captured using a Leica SP5 X MP confocal microscope
386 using a 40x Leica objective, with excitation and emission at 488 and 509 nm for GFP, and 575 and
387 650 nm for mCherry.

388 Synthesis of RNA-binding peptides, RNA aptamers, and electrophoretic mobility shift assay
389 (EMSA)

390 The RNA-binding peptides (Rev–RRRG, P22N–RRRG, λN–RRRG, BTat–RRRG, HTat–
391 RRRG, and Rex–RRRG, Table S2) were synthesized using standard Fmoc solid-phase synthesis
392 at Sangon Biotechnology Company. Briefly, the synthesis of peptides was carried out on
393 ChemMatrix resins using Rink Amide to produce C-terminal amides. For the coupling of amino
394 acids, a pre-activation step was conducted using five equivalents of Fmoc-protected amino acid
395 with 4.9 equivalents of *O*-(benzotriazol-1-yl)-*N*,*N*,*N′*,*N′*-tetramethyluronium hexafluorophosphate
396 (HBTU), five equivalents of N-hydroxybenzotriazole (HOBt), and 10 equivalents of *N*,*N*-
397 diisopropylethylamine (DIPEA) in dimethylformamide (DMF), followed by reaction with the N-
398 terminally deprotected peptidyl resin. Thorough washing of the resin with DMF was executed, and
399 the completion of the reaction was assessed using the Kaiser test. Deprotection of Fmoc was
400 achieved with an excess of 20% (v/v) piperidine in DMF, and the washed deprotected peptidyl
401 resin was rinsed with DMF to eliminate any residual piperidine. Cleavage from the resin along
402 with side-chain deprotection occurred using a mixture of 95% TFA, 2.5% TIS, and 2.5% H_2O at
403 room temperature for 1.5–2 h. The resultant peptide was precipitated using cold diethyl ether,
404 separated via centrifugation, and subsequently dissolved in water containing 0.1% v/v
405 trifluoroacetic acid before undergoing RP–HPLC and ESI–MS analyses.

406 The reverse complementary sequences of RNA aptamers' DNA (RRE, P22N, λN, Pepper,
407 and XBE (Table S8) with *T7* promoter were synthesized and annealed with the *T7* promoter as
408 templates for *in vitro* transcription. The RNA aptamers were *in vitro* transcribed according to the
409 Transcription T7 kit (Cat. 6140, Takara) and labeled with biotin using Pierce™ RNA Biotin
410 Labelling Kit (Cat. 20160, Thermo Scientific).

411 EMSA experiments were performed using a LightShift Chemiluminescent RNA EMSA Kit
412 (Cat. 20158, Thermo Scientific). 3′ biotin-labeled RNA probes and synthesized peptides were
413 incubated in binding buffer (3 mM $MgCl_2$, 40 mM KCl, 5% v/v glycerol, 2 mM DTT, 2 μg tRNA)
414 for 40 min at room temperature, and mobility shift assay was performed using 6% acrylamide
415 native gel electrophoresis. After electrophoresis, gels were sandwiched between filter paper and
416 0.5x TBE buffer-soaked nylon membrane in a clean electrophoretic transfer unit for
417 electrophoretic transfer at 400 mA (~35 V) for 30 min. After UV cross-linking, biotin signals were
418 detected with stabilized streptavidin–horseradish peroxidase conjugate using a Chemiluminescent
419 Nucleic Acid Detection Module (Thermo Fisher Scientific, China).

420 Design of RNA switches

421 RNA switches were designed based on the RRE sequence, containing three functional
422 elements, probe sequence, linker 1, and linker 2. Linkers 1 and 2 hybridize with the RRE and the
423 probe, respectively.

424 Linker 2 is designed as the reverse complementary sequence to the 3′ end of the RRE ligand.
425 Its role is to disrupt the active conformation of the RRE ligand by base-pairing with its 3′ end.
426 Therefore, the linker 2 sequence should be placed at the 5′ end of the RNA switch, allowing it to
427 hybridize with the 5′ end of the RRE ligand, which is critical for maintaining the inactive
428 conformation of the RNA switch. The binding strength between Linker 2 and the RRE ligand
429 should not be excessively strong. If the binding force is too strong and the change of RRE
430 conformation is completely disrupted, the RRE will not be able to revert to its active conformation,
431 even when the probe binds.

432 Linker 1 sequences were introduced, which is designed to be reverse complementary to the
433 3′ end of the probe sequence. Its primary function is to enhance the inactive conformation of the
434 RRE by Linker 2 in the absence of the target RNA. In the presence of the target RNA, the probe
435 binds to the target RNA, triggering the dissociation of linker 1 from the probe. This dissociation
436 further disrupts the binding of linker 2 and the RRE ligand, allowing the RRE to regain active
437 conformation.

438 For probe design, we used Stellaris Probe Designer on Biosearch Technologies
439 (https://www.biosearchtech.com/support/tools/design-software/stellaris-probe-designer) with

440 default settings. The 5′ and 3 UTR regions of target RNAs should be avoided in designing the
441 probe. A probe with an annealing temperature below 65°C and a minimum length of 22 nucleotides
442 is desirable.

443 The structures of RNA switch sequences were predicted by mFold
444 (www.unafold.org/mfold/applications/rna-folding-form.php) with default settings.

445 Expression of RNA switch–RTF in plants

446 The plasmid pCambia1300 was used as a backbone to construct RNA switch-RTF components.
447 The sequences encoding fused GFP–RBP–RRRG proteins were cloned into the plasmid under the
448 *UBQ10* promoter. The sequences for the RNA switch driven by the *AtU6* promoter, with various
449 probes targeting *mCherry*, were cloned in the same plasmid upstream of the *UBQ10* promoter. The
450 RNA switch sequences are listed in Table S9. These types of plasmids were named RNA switch–
451 RTF plasmids (Table S10) and were introduced into the leaves of transgenic *N. benthamiana*
452 *mCherry* lines via agroinfiltration.

453 The RNA switch–RTF plasmid with a probe targeting *CM3* mRNA was introduced into *A.*
454 *thaliana* wild type and *cm3* mutant plants respectively via floral dip. Homozygous T_3 lines were
455 used.

456 Design of RTF–SFP and RTF–SunTag

457 RTF–SFP was modified in the RNA switch–RTF plasmid described above by replacing
458 sequences encoding fused GFP–Rev–RRRG proteins with the sequences of $GFP_{1–10}$ (the GFP β-
459 strand 1-10, which could combine the GFP β-strand 11 to restore GFP signal), an internal ribosome
460 entry site (IRES), and 24× GFP_{11}. These were named RNA switch–RTF–SFP plasmids (Table
461 S10).

462 RTF–SunTag was also modified in the RNA switch–RTF plasmid, by replacing sequences
463 encoding fused GFP–Rev–RRRG proteins with sequences of SunTag–Rev, an internal ribosome
464 entry site (IRES), and GFP–scFv–RRRG. These were named RNA switch–RTF–SunTag plasmids
465 (Table S10).

466 Generation of transgenic *A. thaliana* plants expressing various RNA switch–RTFst constructs

467 A series of RNA switch–RTF–SunTag (RNA switch–RTFst) plasmids with various probe
468 sequences in RNA switches were constructed (Table S9). These were introduced to *A. tumefaciens*
469 GV3101 and transgenic *A. thaliana* lines were generated via the floral-dip method *(2)*, and
470 homozygous lines were used.

471 Single-molecule fluorescence *in situ* hybridization

472 For probe design, five probes targeting various sites of the *CM3* coding region were designed
473 using Stellaris® Probe Designer version 2.0 from Biosearch Technologies
474 (http://singlemoleculefish.com). Before ordering pre-labeled probes from Biosearch Technologies,
475 a TAIR BLAST query was run for each sequence to ensure target specificity
476 (https://www.arabidopsis.org/Blast/). The oligonucleotides of each probe, labeled with Cy3 at the
477 5′ terminus, were synthesized by Sangon Biotech Co., Ltd..

478 For sample preparation, root tips of 10-d-old transgenic seedlings were collected and fixed in
479 2-(N-morpholino) ethane sulfonic acid (MES) buffer, pH 5.7, containing 4% v/v
480 paraformaldehyde for 30 min at room temperature. The roots were rinsed twice with 1× PBS and
481 placed onto a microscope slide with a coverslip, gently squashed and briefly submerged in liquid
482 nitrogen. The coverslips were then removed, and the samples were left to dry at room temperature
483 for 30 min. Tissue permeabilization was carried out by immersing the samples in Coplin jars
484 containing 70% v/v ethanol, which were shaken gently for at least 1 h. The ethanol was evaporated
485 at room temperature before the roots were washed twice with MES.

486 Hybridization was performed as previously described (*3*). Briefly, 100 μL of hybridization
487 solution with probes at a final concentration of 250 nM was added to each slide. Coverslips were
488 placed over the samples to prevent buffer evaporation, and the probes were left to hybridize in a
489 humid chamber at 37°C overnight in the dark. The samples were washed twice for 45 min at 37°C
490 with freshly prepared 1× SSC/40% v/v formamide buffer, rinsed at room temperature with MES
491 buffer (pH 5.8), and dried. A drop of ProLong Diamond Antifade Mountant (Invitrogen)
492 containing DAPI was added prior to observation.

493 Construction of MCP–MS2 system and dCas9-SunTag system

494 The DNA sequence of 24× MS2 was cloned into the 3′ UTR of *CM3* under control of the
495 *UBQ10* promoter to form a fused CM3–24×MS2 expression plasmid. The DNA encoding fused

496 mCherry–MCP was cloned into the plasmid under the *UBQ10* promoter. The DNA of dCas9-
497 SunTag were synthesized and subsequently inserted downstream the *UBQ10* promoter in a
498 pCAMBIA1300s plasmids containing a cognate sgRNA expression cassette.

499 Protoplast isolation and imaging

500 *Agrobacteria* containing RNA switch–RTF–SunTag plasmids were co-transformed into
501 tobacco epidermal cells with containing CM3–24×MS2 plasmids and the mCherry–MCP plasmid
502 by agroinfiltration as described above. Twenty-eight hours after infiltration, leaves were cut off
503 for protoplast isolation based on a described previously protocol [61]. Images were taken using a
504 Leica SP5 X MP confocal microscope using a 40x Leica objective, with excitation and emission
505 at 488 and 509 nm for GFP, and 575 and 650 nm for mCherry.

506 Estimating the proximity of RNAs to mitochondria

507 *Nicotiana benthamiana* leaves were agroinfiltrated with constructs expressing RNA switch-
508 RTF-SunTag and mitochondrial-targeting RNA *VDAC3*. Twenty-eight hours after infiltration,
509 leaves were infiltrated with 1 μM MitoTracker® Red CMXRos (ThermoFisher, A66443) for
510 mitochondria labeling. The movements of *VDAC3* RNA particles to mitochondria in living
511 epidermal cells were captured using confocal microscopy time-lapse imaging. The distance from
512 the center of each *VDAC3* RNA particle to the center of the closest mitochondrion is measured
513 with ImageJ and the number of particles at a given mitochondrion distance is calculated [44].

514 Western blotting

515 Total protein extraction and western blotting were performed as previously described (*5*).
516 Briefly, protein extracts were mixed with SDS–PAGE sample buffer and denatured at 95°C for 5
517 min. After brief centrifugation, denatured protein samples were separated by 12% SDS–PAGE
518 and blotted onto PVDF membranes. Primary and secondary antibodies were used at the following
519 dilutions: 1:10,000 for GFP (ab290; Abcam), 1:10,000 for ubiquitin (MAB3408; Sigma-Aldrich),
520 and 1:10,000 for anti-IgG (mouse) HRP conjugate (W402B; Promega). Immunoreactive bands
521 were visualized using ImmunoStar® LD (Wako).

522 Microscopy setup and image acquisition

523 For protoplast imaging, protoplasts were stained with 100 μM FM4-64 for 1 min and washed
524 with W5 solution before imaging. For epidermal-cell imaging, agroinfiltrated *N. benthamiana*

525 leaves were cut for imaging 72 h after agroinfiltration. For mitochondrial localization,
526 agroinfiltrated leaves were incubated with 200 nM MitoTracker red CMXRos in 1× PBS buffer
527 with 3% w/v sucrose for 15 min before imaging (*6*). Images were captured on a spinning-disk
528 confocal microscope (Olympus SpinSR10) with an EMCCD camera and 40× oil objective. GFP,
529 Cy3, DAPI, FM4-64 and MitoTracker red CMXRos signals were detected at respective
530 excitation/emission wavelengths of 488/498–559 nm, 554/568 nm, 405/420–480 nm, 488/734 nm
531 and 561 nm/580–625 nm. Panoramic images of tissues were acquired with the Olympus VS200
532 panoramic digital scanner (Japan). For visualization of *TUB5* expression during plant growth, GFP
533 signal in whole plants was acquired using NightShade LB 985 In vivo Plant Imaging System
534 (Berthold) every two weeks throughout the growth period. For detection of *TCTP1* mRNA long-
535 distance movement, Arabidopsis rootstock samples at different distances from the graft junction
536 were cut for Z-stack image acquisition using a spinning-disk confocal microscope (Olympus
537 SpinSR10) with an EMCCD camera and 20× objective. For observation of the cell-to-cell
538 movement of *TCTP1* mRNA, time-lapse imaging of elongation-region cells of rootstock roots was
539 performed using a SpinSR10 microscope with a 20× objective every 3 sec for 1 min.

540 RT–qPCR

541 Total RNA was extracted using the Qiagen RNeasy kit, following the manufacturer's
542 instructions. Reverse transcription was performed with 1 μg RNA using the Qiagen Omniscript kit
543 with a primer mix of random 10 mers (final concentration of 10 μM) and 15 mers oligo dT primers
544 (final concentration of 1 μM). A negative control was performed by adding water instead of reverse
545 transcriptase. For gene expression profiling, qPCR was performed with gene-specific qPCR
546 primers. Ct readouts of each gene were first normalized to the housekeeping gene *β-Actin* (Δ Ct),
547 and the relative expression of individual genes versus the expression levels in control conditions
548 was then calculated with the $2^{-\Delta\Delta Ct}$ method. Primers are listed in Table S7.

549 Micro-grafting of *A. thaliana* plants

550 *Arabidopsis thaliana* seeds were germinated and grown vertically on plates containing 1/2
551 MS salts, 1% w/v sucrose, and 1% w/v micro agar under short-day conditions in a controlled-
552 environment chamber (Percival) for one week. Micro-grafting of seedlings was performed as
553 described (*7*). Briefly, seedlings of similar sizes and with evenly elongated hypocotyls were cut in
554 the upper half of the hypocotyl with a sterilized razor blade. The junctions of the graft were

supported using silicon microtubing (0.3-mm internal diameter). Grafted plants were then transferred to new plates and grown vertically under short-day conditions. Adventitious roots that formed above the junction were removed every 2 d.

Aphid feeding experiments

Ya1-targeted RNA switch–RTFst plasmids were agroinfiltrated into four-week-old *N. benthamiana* leaves. Forty-eight hours post-infiltration, five aphids were confined to the infiltration zone using rubber bands and double-sided tape to prevent escape. After 24 h of feeding, leaf samples were collected for confocal fluorescence microscopy using an Olympus FV3000. Additionally, co-infiltration of full-length *Ya1* plasmids with *Ya1*-targeted RNA switch-RTFst plasmids was performed.

Leaf discs (4 cm^2) containing agroinfiltrated switch–RTFst plasmid constructs were excised 48 h post-infiltration and transferred to six-well plates containing Murashige and Skoog (MS) liquid medium to maintain osmotic balance and humidity. Aphids (3–4 individuals) were introduced onto the leaf discs, followed by incubation in controlled growth chambers (25°C, 16/8 h light/dark). Time-lapse imaging was conducted at hourly intervals using an Olympus SpinSR10 spinning-disk confocal microscope, equipped with an automated stage scanning system for panoramic imaging.

Data availability

All data are available in the main text or the supplementary materials. All materials (seed stocks, plasmids) are available upon request.

References

1. Hani, S. et al. Live single-cell transcriptional dynamics via RNA labelling during the phosphate response in plants. *Nat. Plants* **7**, 1050-1064 (2021).
2. López-Maury, L., Marguerat, S., and Bähler, J. Tuning gene expression to changing environments: from rapid responses to evolutionary adaptation. *Nat. Rev. Genet.* **9**, 583-593 (2008).
3. Huang, N. C., Luo, K. R., and Yu, T. S. Development of a split fluorescent protein-based RNA live-cell imaging system to visualize mRNA distribution in plants. *Plant Methods* **18**, 1-10 (2022).
4. Alamos, S. et al. Quantitative imaging of RNA polymerase II activity in plants reveals the single-cell basis of tissue-wide transcriptional dynamics. *Nat. Plants* **7**, 1037-1049 (2021).
5. Kitagawa, M., Tran, T. M., and Jackson, D. Traveling with purpose: cell-to-cell transport of plant mRNAs. *Trends Cell Biol.* **34**, 48-57 (2024).

588 6. Liu, L. and Chen, X. Intercellular and systemic trafficking of RNAs in plants. *Nat. Plants* **4**,
589 869-878 (2018).

590 7. Zhang, W. et al. Graft-transmissible movement of inverted-repeat-induced siRNA signals into
591 flowers. *Plant J.* **80**, 106-121 (2014).

592 8. Molnar, A. et al. Small silencing RNAs in plants are mobile and direct epigenetic modification
593 in recipient cells. *Science* **328**, 872-875 (2010).

594 9. Corbesier, L. et al. FT protein movement contributes to long-distance signaling in floral
595 induction of Arabidopsis. *Science* **316**, 1030-1033 (2007).

596 10. Han, W. H. et al. A small RNA effector conserved in herbivore insects suppresses host plant
597 defense by cross-kingdom gene silencing. *Mol. Plant* **18**, 437-456 (2025).

598 11. Zhang, Z. L. et al. Cross-kingdom RNA interference mediated by insect salivary microRNAs
599 may suppress plant immunity. *Proc. Natl. Acad. Sci. USA* **121**, e2318783121 (2024).

600 12. Westwood, J. H. and Kim, G. RNA mobility in parasitic plant - host interactions. *RNA Biol.*
601 **14**, 450-455 (2017).

602 13. van Kleeff, P. J. et al. Small RNAs from Bemisia tabaci Are Transferred to Solanum
603 lycopersicum Phloem during Feeding. *Front Plant Sci.* **7**, 1-12 (2016).

604 14. Wang, M., Thomas, N., and Jin, H. Cross-kingdom RNA trafficking and environmental RNAi
605 for powerful innovative pre- and post-harvest plant protection. *Curr. Opin. Plant Biol.* **38**,
606 133-141 (2017).

607 15. Bai, J. et al. A protein-independent fluorescent RNA aptamer reporter system for plant genetic
608 engineering. *Nat. Commun.* **11**, 3847 (2020).

609 16. Chen, X. J. et al. Visualizing RNA dynamics in live cells with bright and stable fluorescent
610 RNAs. *Nat. Biotechnol.* **37**, 1287-1293 (2019).

611 17. Haimovich, G. et al. Use of the MS2 aptamer and coat protein for RNA localization in yeast:
612 A response to "MS2 coat proteins bound to yeast mRNAs block 5′ to 3′ degradation and trap
613 mRNA decay products: implications for the localization of mRNAs by MS2-MCP system".
614 *RNA* **22**, 660-666 (2016).

615 18. Garcia, J. F. and Parker, R. Ubiquitous accumulation of 3′ mRNA decay fragments in mRNAs
616 with chromosomally integrated MS2 arrays. *RNA* **22**, 657-659 (2016).

617 19. Garcia, J. F. and Parker, R. MS2 coat proteins bound to yeast mRNAs block 5′ to 3′
618 degradation and trap mRNA decay products: implications for the localization of mRNAs by
619 MS2-MCP system. *RNA* **21**, 1393-1395 (2015).

620 20. Park, H. Y. et al. Visualization of Dynamics of Single Endogenous mRNA Labeled in Live
621 Mouse. *Science* **343**, 422-424 (2014).

622 21. Göhring, J., Jacak, J., and Barta, A. Imaging of Endogenous Messenger RNA Splice Variants
623 in Living Cells Reveals Nuclear Retention of Transcripts Inaccessible to Nonsense-Mediated
624 Decay in Arabidopsis. *Plant Cell* **26**, 754-764 (2014).

625 22. Wang, Z. J. et al. In Situ Spatial Complementation of Aptamer-Mediated Recognition Enables
626 Live-Cell Imaging of Native RNA Transcripts in Real Time. *Angewandte Chemie-*
627 *International Edition* **57**, 972-976 (2018).

628 23. Xia, C. et al. Single-molecule live-cell RNA imaging with CRISPR-Csm. *Nat Biotechnol.* **1**,
629 1-21 (2025).

630 24. Colognori, D., Trinidad, M., and Doudna, J. A. Precise transcript targeting by CRISPR-Csm
631 complexes. *Nat Biotechnol.* **41**, 1256-1264 (2023).

632 25. Yang, L. Z. et al. Dynamic Imaging of RNA in Living Cells by CRISPR-Cas13 Systems. *Mol.*
633 *Cell* **76**, 981-997 (2019).

634 26. Nelles, D. A. et al. Programmable RNA Tracking in Live Cells with CRISPR/Cas9. *Cell* **165**,
635 488-496 (2016).

636 27. Le, P., Ahmed, N., and Yeo, G. W. Illuminating RNA biology through imaging. *Nat. Cell Biol.*
637 **24**, 815-824 (2022).

638 28. Liu, Y. et al. A split ribozyme system for in vivo plant RNA imaging and genetic engineering.
639 *Plant Biotechnol. J.* **1**, 1-10 (2025).

640 29. Yang, L. et al. m^5C Methylation Guides Systemic Transport of Messenger RNA over Graft
641 Junctions in Plants. *Curr. Biol.* **29**, 2465-2476 (2019).

642 30. Chen, Y. Z. et al. An aphid RNA transcript migrates systemically within and is a virulence
643 factor. *P. Natl. Acad. Sci. USA* **117**, 12763-12771 (2020).

644 31. Chen, X. Y. et al. Molecular basis for arginine C-terminal degron recognition by $Cul2^{FEM1}$ E3
645 ligase. *Nat. Chem. Biol.* **17**, 1552-4450 (2021).

646 32. Sepers, J. J. et al. The mIAA7 degron improves auxin-mediated degradation in
647 Caenorhabditiselegans. *G3 (Bethesda)* **12**, 1-15 (2022).

648 33. Yesbolatova, A. et al. Generation of conditional auxin-inducible degron (AID) cells and tight
649 control of degron-fused proteins using the degradation inhibitor auxinole. *Methods* **164**, 73-
650 80 (2019).

651 34. Austin, R. J. et al. Designed arginine-rich RNA-binding peptides with picomolar affinity. *J.*
652 *Am. Chem. Soc.*, 10966-10967 (2002).

653 35. Smith, C. A., Calabro, V., and Frankel, A. D. An RNA-Binding Chameleon. *Mol. Cell* **6**, 1067-
654 1076 (2000).

655 36. Jiang, F. et al. Anchoring an extended HTLV-1 Rex peptide within an RNA major groove
656 containing junctional base triples. *Structure*, 1461-S12 (1999).

657 37. Legault, P. et al. NMR Structure of the Bacteriophage λ N Peptide/boxB RNA Complex:
658 Recognition of a GNRA Fold by an Arginine-Rich Motif. *Cell* **93**, 289-299 (1998).

659 38. Battiste, J. L. et al. Alpha helix-RNA major groove recognition in an HIV-1 rev peptide-RRE
660 RNA complex. *Science* **273**, 1547-1551 (1996).

661 39. Puglisi, J. D. et al. Solution Structure of a Bovine Immunodeficiency Virus Tat-TAR Peptide-
662 RNA Complex. *Science* **270**, 1200-1203 (1995).

663 40. Chen, M. et al. Live imaging of RNA and RNA splicing in mammalian cells via the dcas13a-
664 SunTag-BiFC system. *Biosens. Bioelectron.* **204**, 1-11 (2022).

665 41. Luo, K., Huang, N., and Yu, T. Selective Targeting of Mobile mRNAs to Plasmodesmata for
666 Cell-to-Cell Movement. *Plant Physiol.*, 604-614 (2018).

667 42. Biayna, J. and Dumbović, G. Decoding subcellular RNA localization one molecule at a time.
668 *Genome Biol* **26**, 1-23 (2025).

669 43. Fischer, A. et al. Membrane localization of acetylated CNK1 mediates a positive feedback on
670 RAF/ERK signaling. *Sci. Adv.* **3**, 1-10 (2017).

671 44. Michaud, M. et al. Differential targeting of VDAC3 mRNA isoforms influences mitochondria
672 morphology. *P. Natl. Acad. Sci. USA* **111**, 8991-8996 (2014).

673 45. Bach-Pages, M. et al. Discovering the RNA-Binding Proteome of Plant Leaves with an
674 Improved RNA Interactome Capture Method. *Biomolecules* **10**, 1-21 (2020).

46. Zheng, L. L. et al. A root cap-localized NAC transcription factor controls root halotropic response to salt stress in Arabidopsis. *Nat. Commun.* **15**, 1-12 (2024).

47. de los Reyes, P. et al. CONSTANS alters the circadian clock in Arabidopsis thaliana. *Mol. Plant* **17**, 1204-1220 (2024).

48. Gu, S. B. et al. The kinase CIPK11 functions as a positive regulator in cadmium stress response in Arabidopsis. *Gene* **772**, 1-9 (2021).

49. Kondhare, K. R., Patil, N. S., and Banerjee, A. K. A historical overview of long-distance signalling in plants. *J. Exp. Bot.* **72**, 4218-4236 (2021).

50. Wang, S. et al. Plant mRNAs move into a fungal pathogen via extracellular vesicles to reduce infection. *Mol. Plant Microbe In.* **37**, 29-29 (2024).

51. Braselmann, E. et al. Illuminating RNA Biology: Tools for Imaging RNA in Live Mammalian Cells. *Cell Chem. Biol.* **27**, 891-903 (2020).

52. Prigodich, A. E. et al. Nano-flares for mRNA Regulation and Detection. *ACS Nano* **3**, 2147-2152 (2009).

53. Pham, T. G. and Wu, J. H. Recent advances in methods for live-cell RNA imaging. *Nanoscale* **16**, 5537-5545 (2024).

54. Al Mazid, M. F. et al. Application of fluorescent turn-on aptamers in RNA studies. *Mol. Omics* **17**, 483-491 (2021).

55. Truong, L. and Ferré-D'Amaré, A. R. From fluorescent proteins to fluorogenic RNAs: Tools for imaging cellular macromolecules. *Protein Sci.* **28**, 1374-1386 (2019).

56. Singh, V. and Jain, M. Recent advancements in CRISPR-Cas toolbox for imaging applications. *Crit. Rev. Biotechnol.* **42**, 508-531 (2022).

57. Chen, A. et al. Improving RNA-based crop protection through nanotechnology and insights from cross-kingdom RNA trafficking. *Curr. Opin. Plant. Biol.* **76**, 1-22 (2023).

58. Weiberg, A. et al. Fungal Small RNAs Suppress Plant Immunity by Hijacking Host RNA Interference Pathways. *Science* **342**, 118-123 (2013).

59. Fan, W. et al. Proteomics integrated with metabolomics: analysis of the internal causes of nutrient changes in alfalfa at different growth stages. *BMC Plant Biol.* **18**, 1-15 (2018).

60. Demichev, V. et al. DIA-NN: neural networks and interference correction enable deep proteome coverage in high throughput. *Nat. Methods* **17**, 41-44 (2020).

61. Yoo, S. D., Cho, Y. H., and Sheen, J. Arabidopsis mesophyll protoplasts: a versatile cell system for transient gene expression analysis. *Nat. Protoc.* **2**, 1565-72 (2007).

Acknowledgments

We sincerely thank Professor Yuelin Zhang (Sichuan University) for his insightful discussions and critical reading of the manuscript. We also appreciate Dr. Yiliang Ding (John Innes Centre, UK) and Dr. Xiaofei Yang (Center for Excellence in Molecular Plant Sciences, Chinese Academy of Sciences, China) for their valuable suggestions.

Funding:

National Natural Science Foundation of China (Grant Nos. 32201241 to JB)

National Natural Science Foundation of China (Grant Nos. 32171457 to YZ)

National Natural Science Foundation of China (Grant Nos. 22325406 to JL)

China Postdoctoral Science Foundation (Grant No. 2022M722280 to JB)

Hubei Hongshan Laboratory (Grant No. 2022hszd026 to YC)

Fundamental Research Funds for the Central Universities (Grant No. 2022ZKPY003 to YC)

Author contributions:

Conceptualization: JB, YZ, YC, CF

Methodology: JL, SP, YT, ML

Investigation: JB, JZ, HR

Visualization: SL, JY, MD, FC

Funding acquisition: JB, YZ, YC, JL

Project administration: YZ, CF

Supervision: YZ, CF

Writing – original draft: JB

Writing – review & editing: YC, YZ, CF

Competing interests: The authors declare no competing interests.

Figures

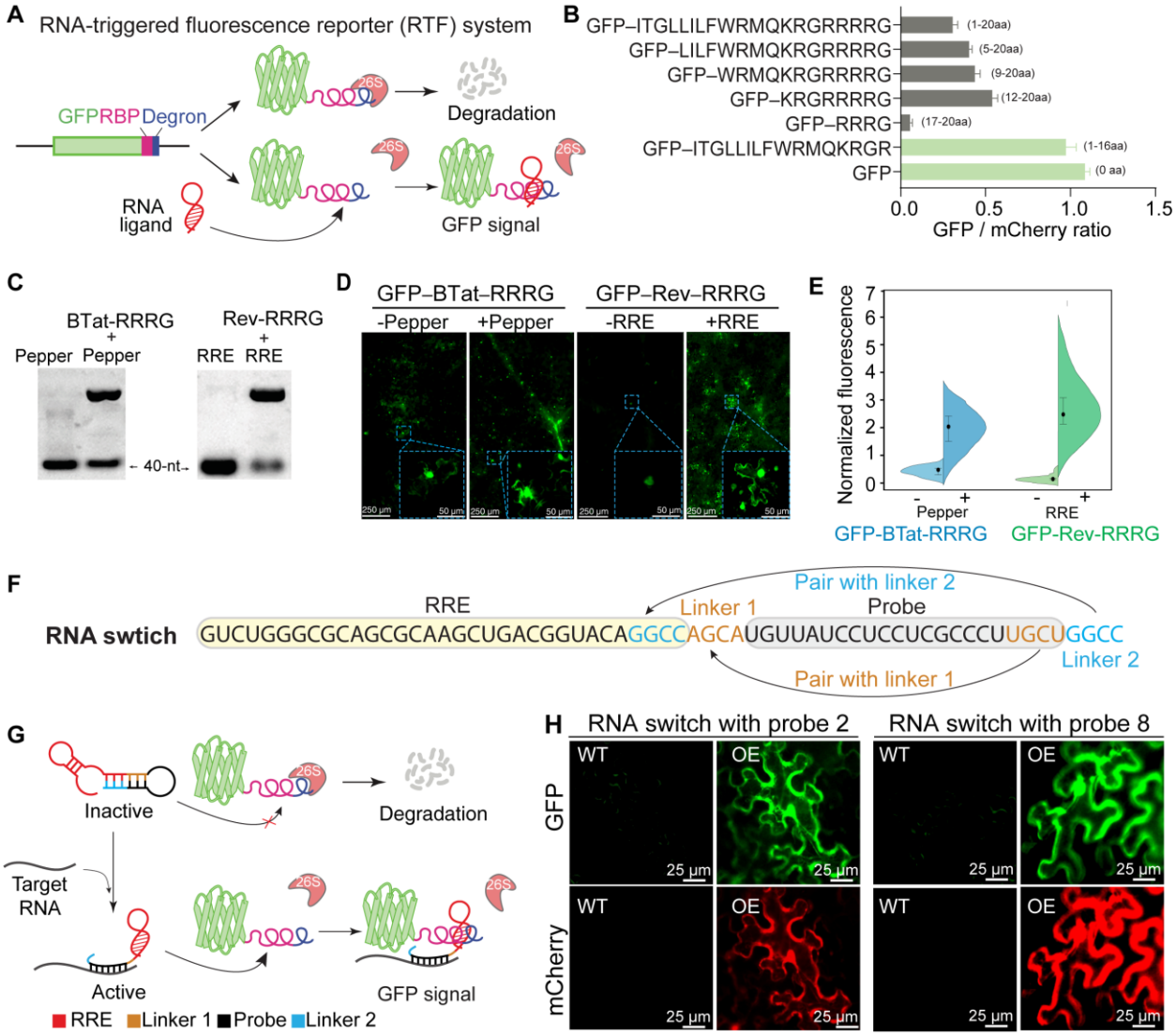

Fig. 1. Design of the RNA switch-controlled RTF system.

(**A**) Schematic of the RTF reporter system. The fusion protein GFP–RBP–Degron undergoes degradation in the absence of RNA ligands. Binding of the RNA ligand to the RBP in the fusion protein blocks accessibility to the 26S proteasome, resulting in GFP signal accumulation. (**B**) Assessment of the degradation ability of putative degron sequences. Degradation efficiency was evaluated based on the GFP/mCherry fluorescence intensity ratio. mCherry and GFP tagged with the putative degron sequence were co-expressed using a 2A self-cleaving peptide system (Fig. S1A). The mCherry–2A–GFP–degron construct was cleaved at the 2A site, producing separate mCherry and GFP–degron proteins. (**C**) Binding abilities of BTat–RRRG and Rev–RRRG to their specific RNA ligands, Pepper and RRE, respectively. (**D** and **E**) GFP fluorescence signals in the

746 absence and presence of specific RNA ligands when tagged with BTat–RRRG or Rev–RRRG. (**F**)
747 Design of the RNA switch. Sequences shaded in yellow comprise the RRE and in gray are the
748 probe. The sequences in brown are linker 1 and those in blue are linker 2. (**G**) Diagram of the RNA
749 switch-controlled RTF reporter system. In the absence of the target RNA, the RNA switch adopts
750 an inactive state through base pairing between linkers and their complementary nucleotides in the
751 probe and RRE. When the target RNA is present, the probe hybridizes with the target, unfolding
752 the RNA switch and enabling it to bind the RBP in GFP–RBP–RRRG. (**H**) RNA switches
753 containing probes 2 and 8 that target *mCherry* RNA, are inactive in *N. benthamiana* WT plants
754 but active in transgenic lines expressing *mCherry*.
755
756
757

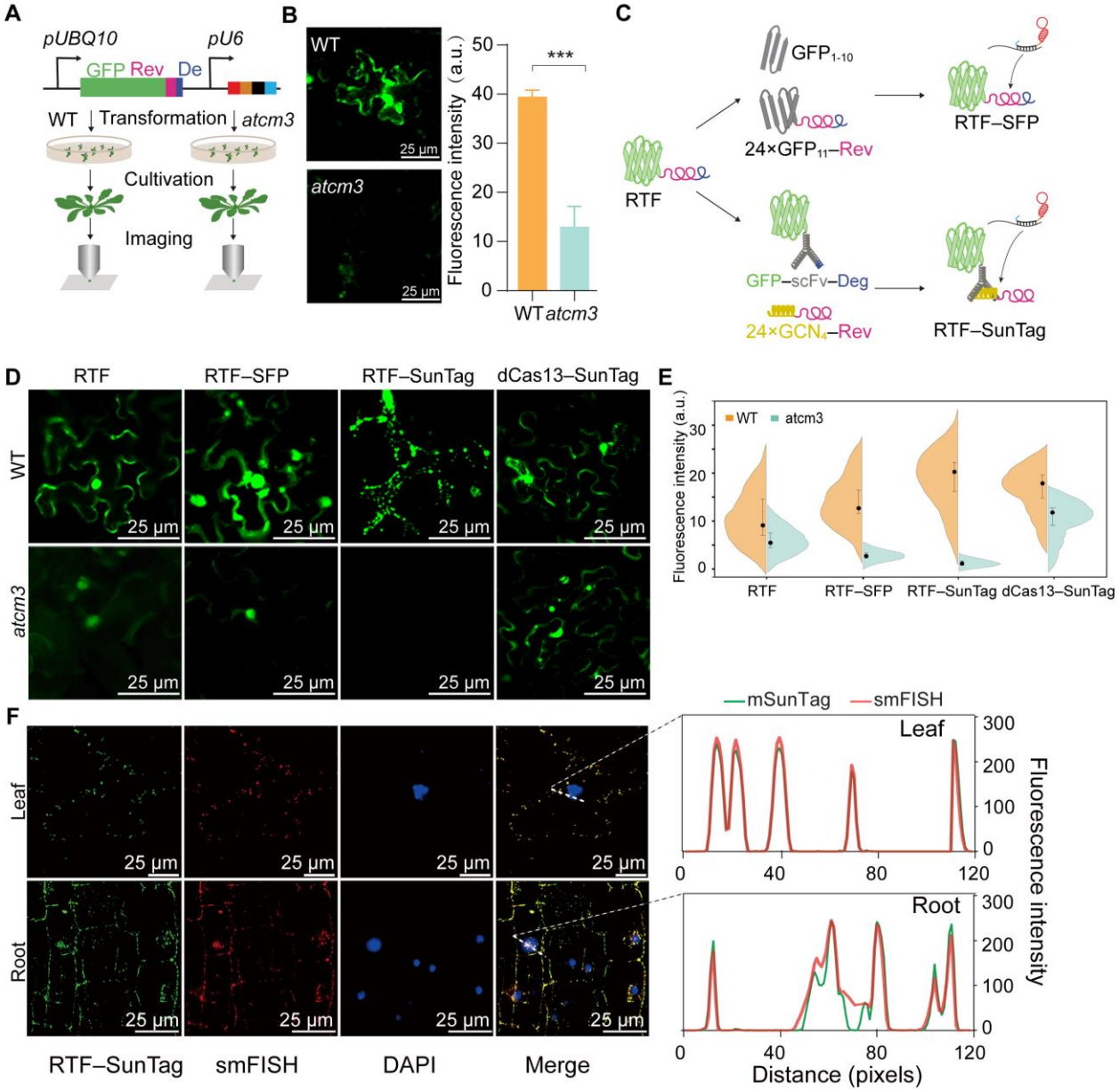

Fig. 2. Optimizing the RNA switch-RTF system in plants.

(**A**) Schematic representation of introducing the RNA switch–RTF system into Arabidopsis. The RTF system, driven by the *UBQ10* promoter, and the RNA switch targeting *CM3* mRNA, driven by the *U6* promoter, are on the same plasmid. The plasmids were introduced into *A. thaliana* WT and *cm3* mutant plants. (**B**) GFP fluorescence signals in WT and *cm3* mutant plants. Left: confocal images. Right: fluorescence intensity. (**C**) Optimizing the GFP reporter by replacing it with a split fluorescent-protein (SFP) approach and SunTag. (**D** and **E**) Fluorescence signals in *A. thaliana* WT and *cm3* mutant plants genetically introduced with RNA switch-controlled RTF, RTF–SFP, RTF–SunTag, and dCas13–SunTag. Confocal images are shown in D and quantification of

768 fluorescence intensity is shown in E. (**F**) Localization of *CM3* mRNA visualized using RNA
769 switch–RTF–SunTag and smFISH. Cy3-labeled probes specific to *CM3* mRNA were used for
770 smFISH. The fluorescence intensity of labeled regions in the merged images is shown on the right.
771 Green lines represent GFP fluorescence intensity, while red lines indicate Cy3 fluorescence
772 intensity.

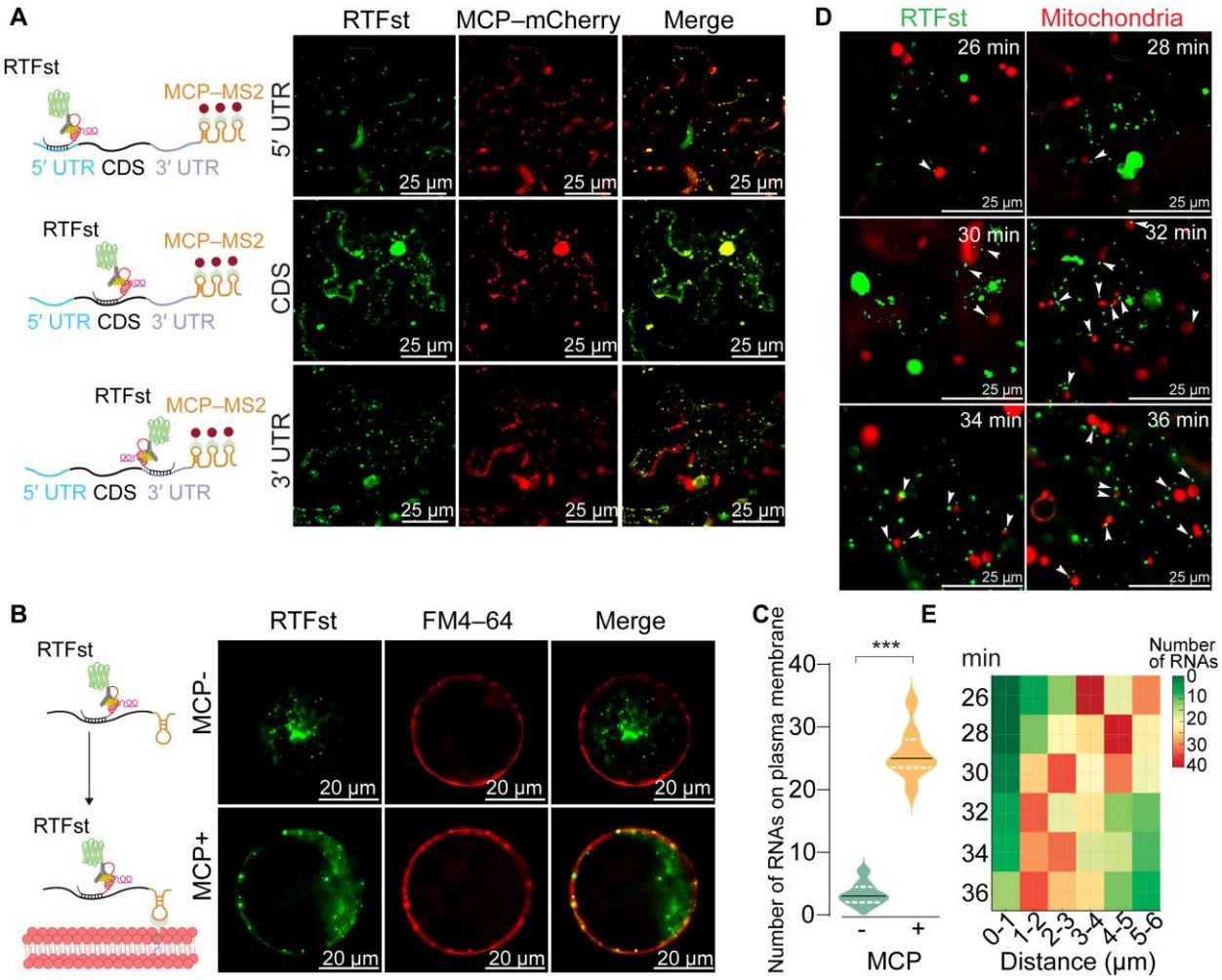

Fig. 3. RNA localization is unaffected by the RNA switch–RTFst complex.

(**A**) RNA localization determined by RNA switch–RTFst is comparable to that assessed by MCP–MS2. The *MCP–MS2* plasmid contains 24× *MS2* loops fused to sequences coding for the 5′ UTR, CDS, and 3′ UTR of *CM3* mRNA, driven by the *UBQ10* promoter, as well as *MCP* sequences driven by the CaMV *35S* promoter. The MCP–MS2 plasmid and the RNA switch–RTFst plasmid with probes targeting the 5′ UTR, CDS, or 3′ UTR were transiently co-expressed in *N. benthamiana* WT leaves. (**B**) The RNA switch–RTFst complex targeting *CM3* mRNA did not obviously affect RNA localization. For the MCP– condition, the RNA switch–RTFst plasmid with a probe targeting the *CM3* coding sequence and a plasmid expressing *CM3–MS2* mRNA were co-expressed in *N. benthamiana* mesophyll protoplasts. For the MCP+ condition, the RNA switch–RTFst plasmid, and the *CM3–MS2* mRNA plasmid containing the *MCP* sequence tagged with CAAX (a membrane targeting motif) were co-expressed in *N. benthamiana* mesophyll protoplasts. Cell membranes were stained with FM4-64. (**C**) Quantification of RNAs localized to the cell

787 membrane. Statistical significance (***$p < 0.001$) was calculated using two-tailed unpaired
788 Student's *t*-test. (**D**) *VDAC3* RNA with the RNA switch–RTFst complex localizes to mitochondria.
789 Green dots represent *VDAC3* RNAs visualized by RNA switch–RTFst, while red dots indicate
790 mitochondria stained with Red CMXRos. White arrows highlight *VDAC3* RNAs in proximity to
791 mitochondria. (**E**) Time-dependent proximity of *VDAC3* RNAs to mitochondria

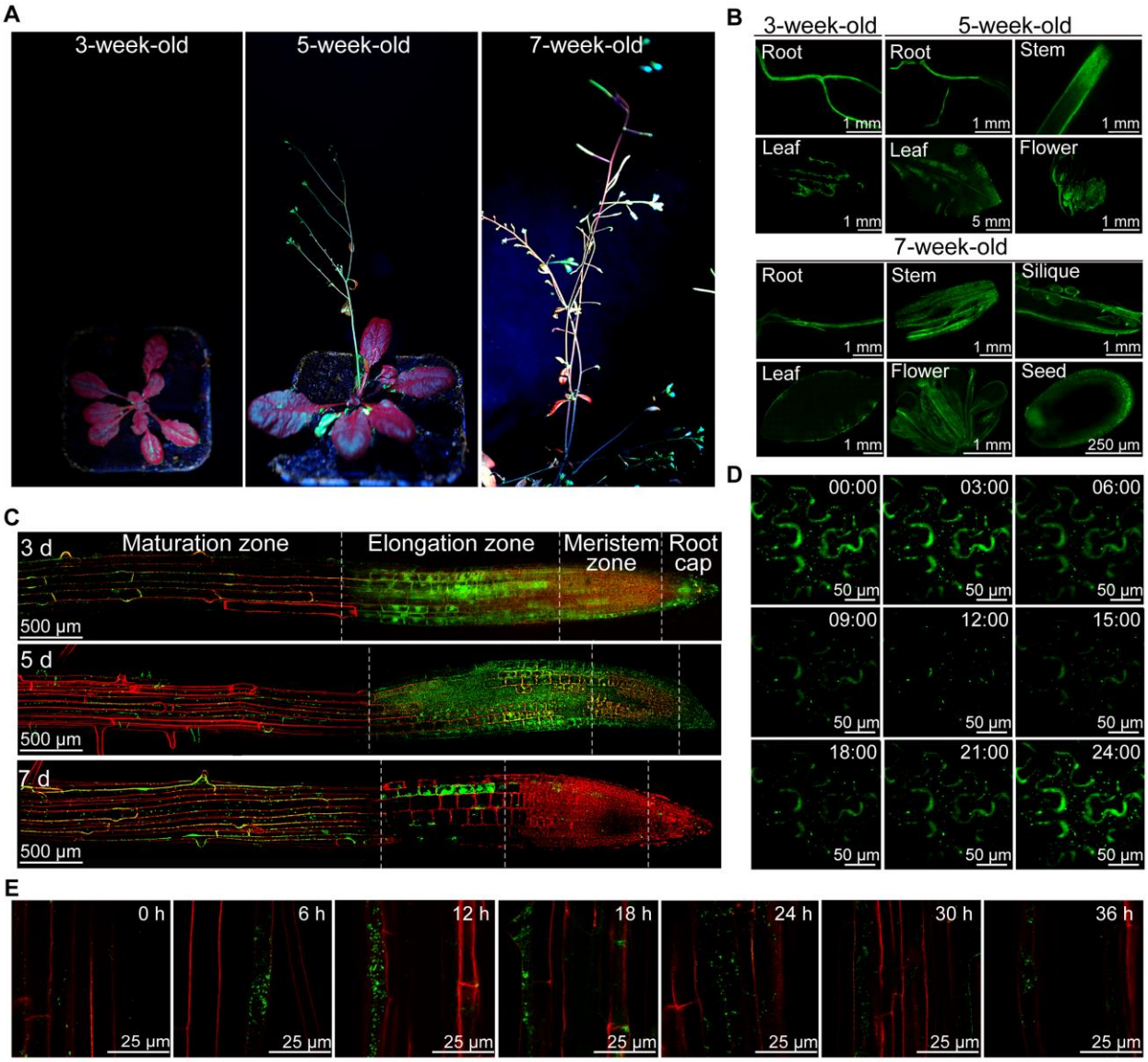

Fig. 4. RNA switch–RTFst enables monitoring dynamic changes in RNA expression at different spatial scales

(**A** and **B**). Developmental stage- (A) and tissue-dependent (B) expression levels of *TUB5*. Transgenic *A. thaliana* plants expressing RNA switch–RTFst targeting *TUB5* RNAs were analyzed. (**C**) Tissue-specific expression patterns of *SMB*. Root tips from transgenic *A. thaliana* plants expressing RNA switch–RTFst targeting *SMB* RNAs were harvested. Cell walls (red) were stained with propidium iodide. (**D**) Circadian-regulated expression patterns of *CCA1*. Leaves from 7-week-old transgenic *A. thaliana* plants expressing RNA switch–RTFst targeting *CCA1* RNAs were collected every 3 h, and GFP signals were observed. (**E**) Cd-induced expression patterns of

803 *CIPK11*. Seven-week-old transgenic *A. thaliana* plants expressing RNA switch–RTFst targeting
804 *CIPK11* RNAs were treated with 50 μM Cd. Roots were harvested every 6 h post-treatment and
805 GFP signals were recorded. Cell walls (red) were stained with propidium iodide. Green
806 fluorescence represents target RNAs visualized by RNA switch–RTFst.
807

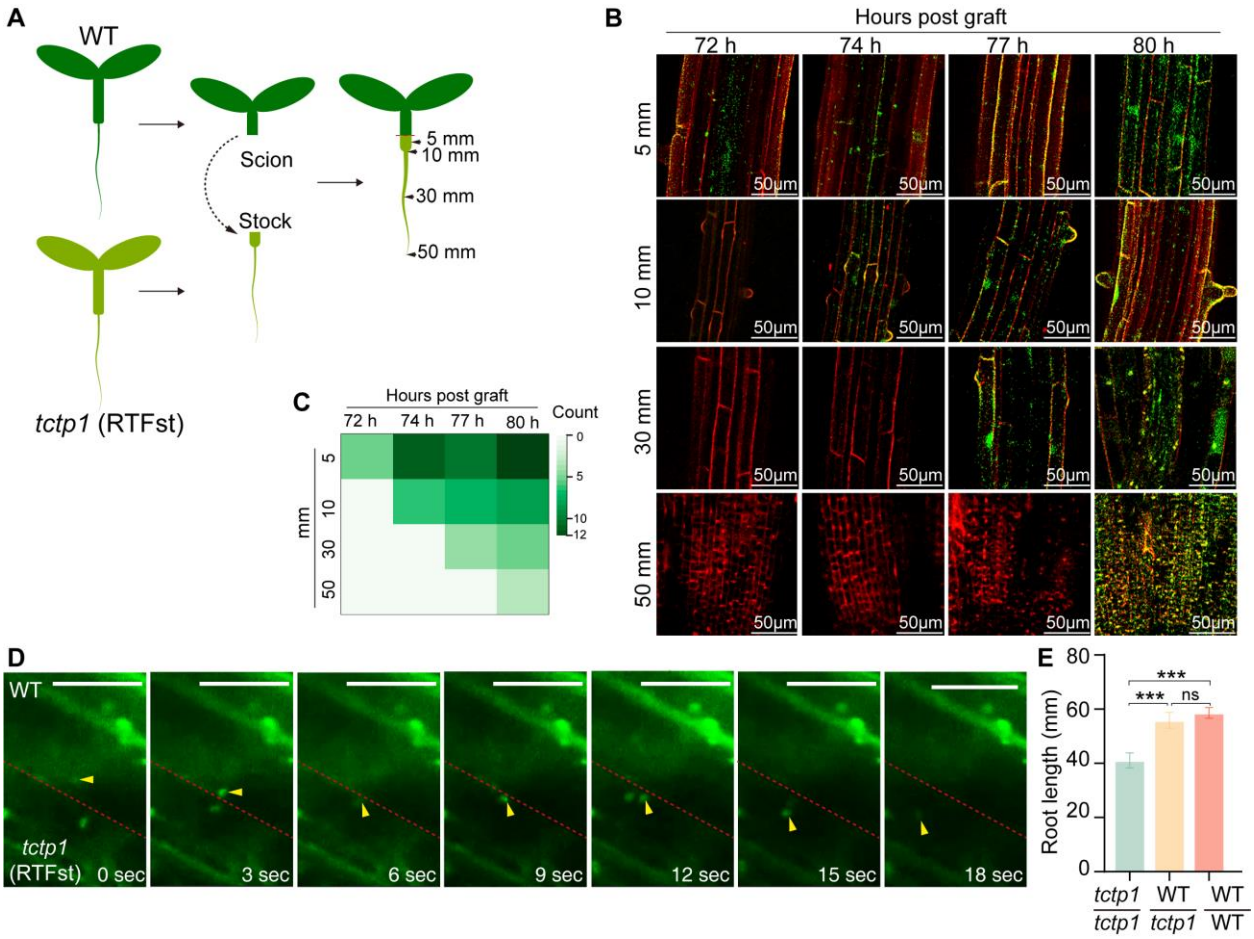

Fig. 5. RNA switch–RTFst visualized the real-time cell-to-cell trafficking of *TCTP1* mRNA.

(**A**) Schematic of hypocotyl grafting. One-week-old Arabidopsis seedlings of similar sizes and with evenly elongated hypocotyls were cut in the upper half of the hypocotyl with a sterilized razor blade. WT shoots were used as scions and *tctp1–RTFst* roots as stocks. The red dashed line indicates the graft junctions. The black arrowhead indicates the positions of 5 mm, 10 mm, 15 mm, and 20 mm below the graft junctions. Grafted plants were grown vertically under short-day conditions. (**B**) Representative imaging of *TCTP1* RNA in different seedlings positions after grafting. Cell walls (red) were stained with propidium iodide. (**C**) Quantification of grafted plants with fluorescence signals at various times post-grafting. Twelve grafted seedlings were imaged for each selected position below the graft junction. (**D**) Real-time fluorescence imaging of cell-to-cell movement of *TCTP1* RNA in root cells of grafted plants. See the **video S1** for details. The red dashed line indicates the cell boundary and the yellow arrowhead indicates *TCTP1* RNA. Scale

821 bar = 25 μm. (**E**) Root length of *tctp1* mutants, grafted plants, WT plants (n = 6, mean ± S.E., ***
822 $P < 0.001$, one-way ANOVA with multiple comparisons and a post-hoc test).

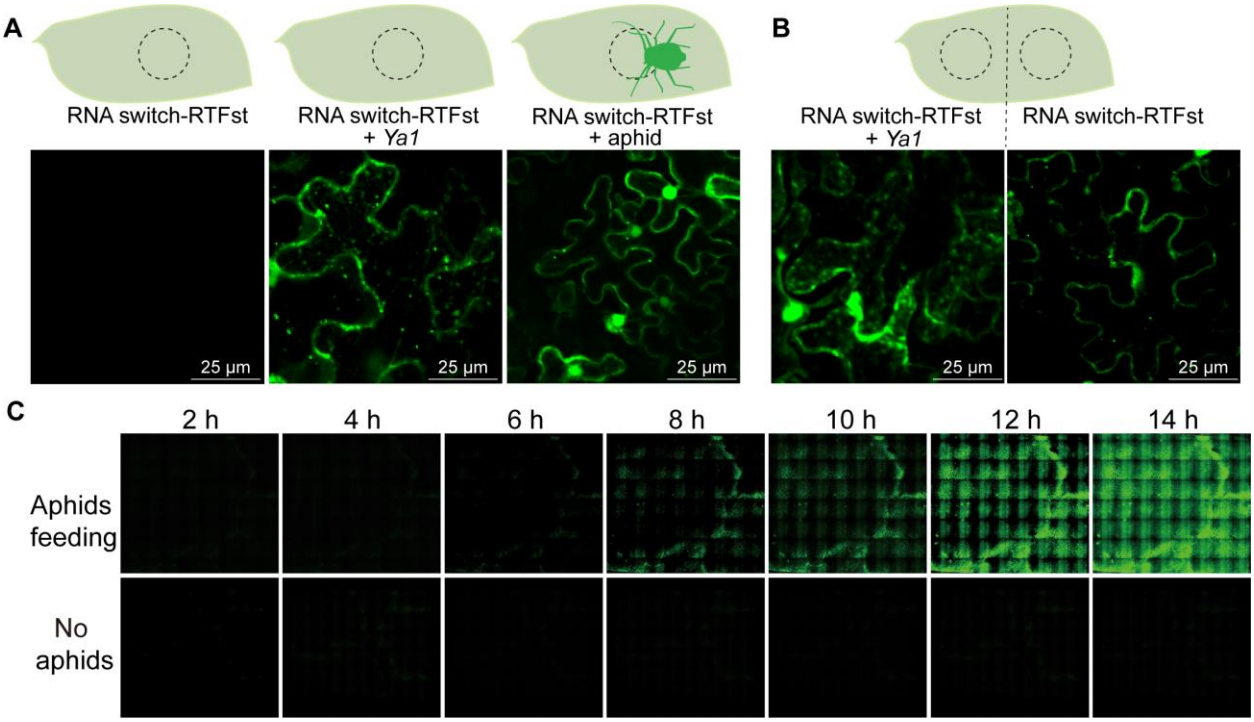

Fig. 6. Aphid-secreted lncRNA *Ya1* is capable of cross-kingdom transfer into leaves of *N. benthamiana*

(**A**) Visualization of the aphid-secreted lncRNA Ya1 in *N. benthamiana* leaves by RNA switch–RTFst. RNA switch–RTFst + *Ya1*, RNA switch–RTFst and *Ya1* were co-expressed via agroinfiltration. RNA switch–RTFst + aphid: aphids fed on *N. benthamiana* leaves in which RNA switch–RTFst was expressed. (**B**) Visualization of cross-cell movement of *Ya1* RNA in *N. benthamiana* leaves (**C**) Visualization of the time-dependent accumulation of Aphid-transferred *Ya1* RNA in *N. benthamiana* leaves using RNA switch–RTFst. Images are panoramic scanning (1cm×1cm) of leaf samples using a confocal fluorescence microscope (Olympus SpinSR10). See **Video S2** for details.

Supplementary Materials for

RNA-triggered fluorescence controlled by RNA switches for real-time RNA expression tracking in living plants

Jiuyuan Bai[1,2]†, Yazhou Chen[3,4]†, Jiayu Zhang[1], Jiang Li[5], Hongpei Ren[1], Shan Pan[1], Yiran Tao[1], Miaomiao Lei[1], Mengyue Dong[1], Sha Liu[1], Jia Yi[1], Fang Chen[1], Chunhai Fan[6]*, Yun Zhao[1]*

†J.B. and Y.C. contributed equally to this work.

*Corresponding author. Email: fanchunhai@sjtu.edu.cn; zhaoyun@scu.edu.cn

The PDF file includes:

Figs. S1 to S5

Tables S1 to S10

References (*1-13*)

Other Supplementary Materials for this manuscript include the following:

Video S1

Video S2

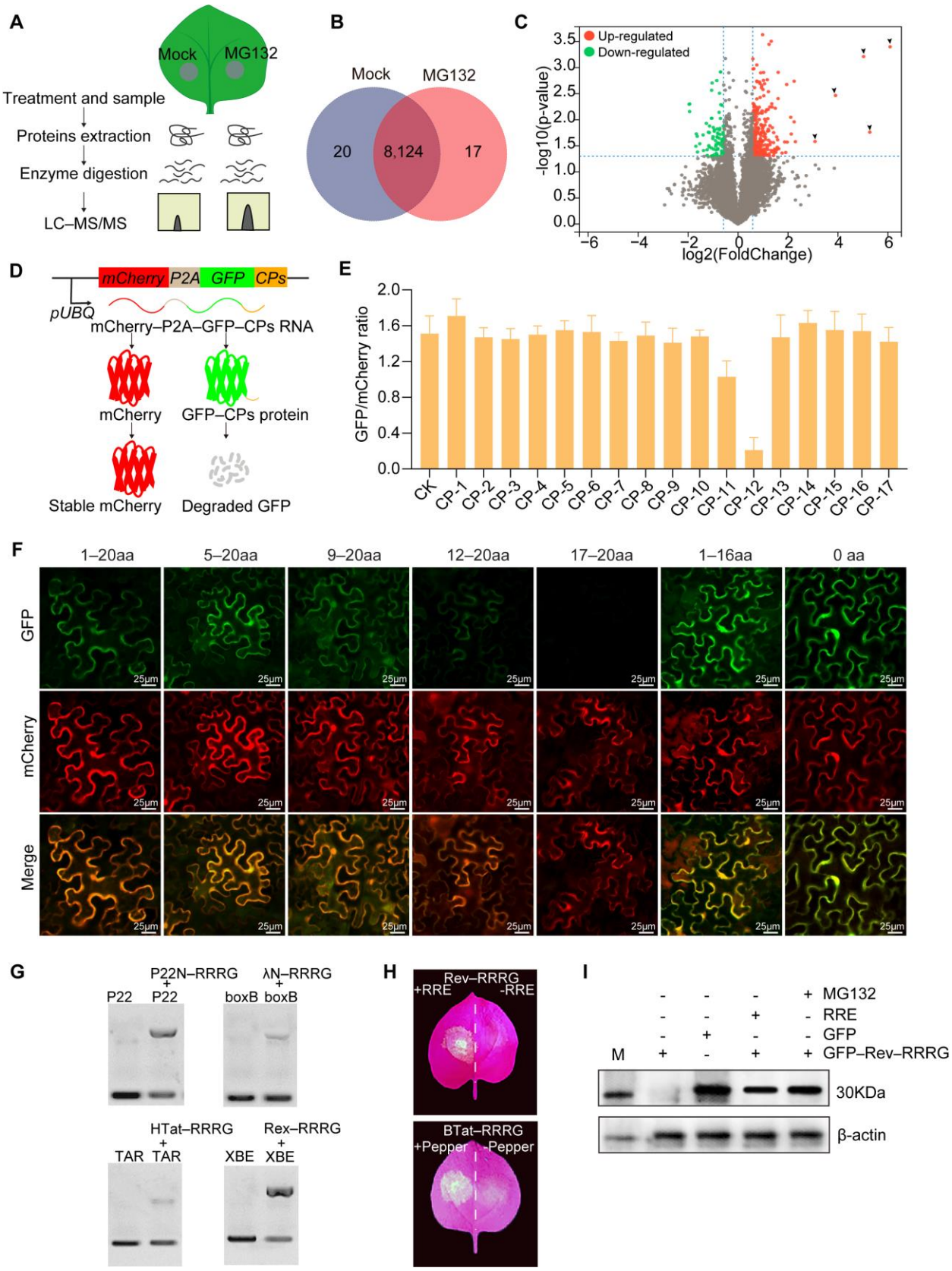

858

859 **Fig. S1.** ***De novo*** **identification of protein degron sequences in** ***N. benthamiana*****.**

860 (**A**) Flowchart showing the identification of constitutively degraded proteins. *Nicotiana*
861 *benthamiana* epidermal cells were infiltrated wither with 10 μM MG132 for 24 h to inhibit
862 proteasome activity or 1× PBS buffer (mock), followed by protein extraction and LC–MS/MS
863 analysis. (**B**) Seventeen proteins were identified in *N. benthamiana* leaves treated with MG132
864 compared to those treated with the mock groups. (**C**) Volcano plot illustrating differentially
865 abundant proteins. (**D**) Schematic of the co-expression system used for fluorescence normalization
866 of GFP fusions. mCherry and GFP, tagged with the putative degron sequence, were co-expressed
867 using a 2A self-cleaving peptide system. CP represents the 20 aa at the C-terminal of 17 proteins
868 detected in MG132-treated leaves. (**E**) Assessment of the effect of CPs on GFP degradation based
869 on the GFP/mCherry fluorescence intensity ratio. CK means control check. (**F**) Representative
870 image showing the effect of different truncations of CP-12 on GFP degradation. Scale bar = 20
871 μm. (**G**) Gel-shift assay testing RNA-binding ability of RBP tagged with the RRRG degron. (**H**)
872 GFP fluorescence signals in the presence and absence of specific RNA aptamers when BTat and
873 Rev are tagged with RRRG. *N. benthamiana* leaves were imaged at 3 d post-agroinfiltration. (**I**)
874 Western blot detection of GFP.
875

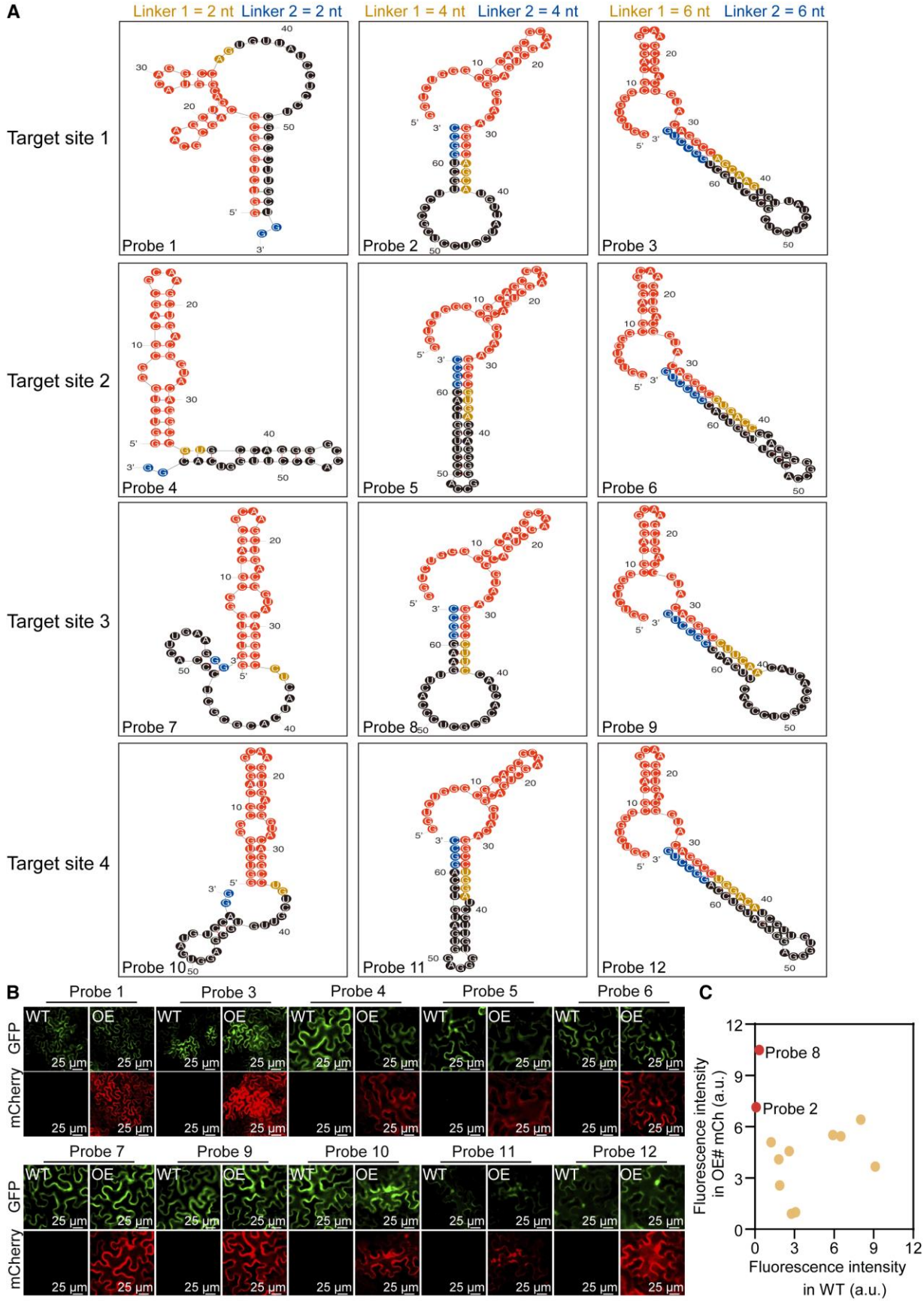
A
Linker 1 = 2 nt Linker 2 = 2 nt
Linker 1 = 4 nt Linker 2 = 4 nt
Linker 1 = 6 nt Linker 2 = 6 nt
Target site 1
Target site 2
Target site 3
Target site 4
Probe 1
Probe 2
Probe 3
Probe 4
Probe 5
Probe 6
Probe 7
Probe 8
Probe 9
Probe 10
Probe 11
Probe 12
B
Probe 1
Probe 3
Probe 4
Probe 5
Probe 6
Probe 7
Probe 9
Probe 10
Probe 11
Probe 12
WT
OE
GFP
mCherry
25 µm
C
Probe 8
Probe 2
Fluorescence intensity in OE# mCh (a.u.)
Fluorescence intensity in WT (a.u.)

876

877 **Fig. S2. Designing of RNA switches targeting *mCherry* RNA.**

878 (**A**) Minimal free energy (MFE) secondary structure of 12 RNA switches (Probes 1–12) designed
879 for specific targeting of *mCherry*. The RNA switches feature linker lengths of 2–6 nt. (**B**)
880 Screening of RNA switches using fluorescent microscopic images of *N. benthamiana* epidermal
881 cells. Scale bars = 50 μm. (**C**) Fluorescence quantification of 12 RNA switches to control RTF
882 reporter expression in WT and *mCherry*-expressing epidermal cells of *N. benthamiana* leaves.

883

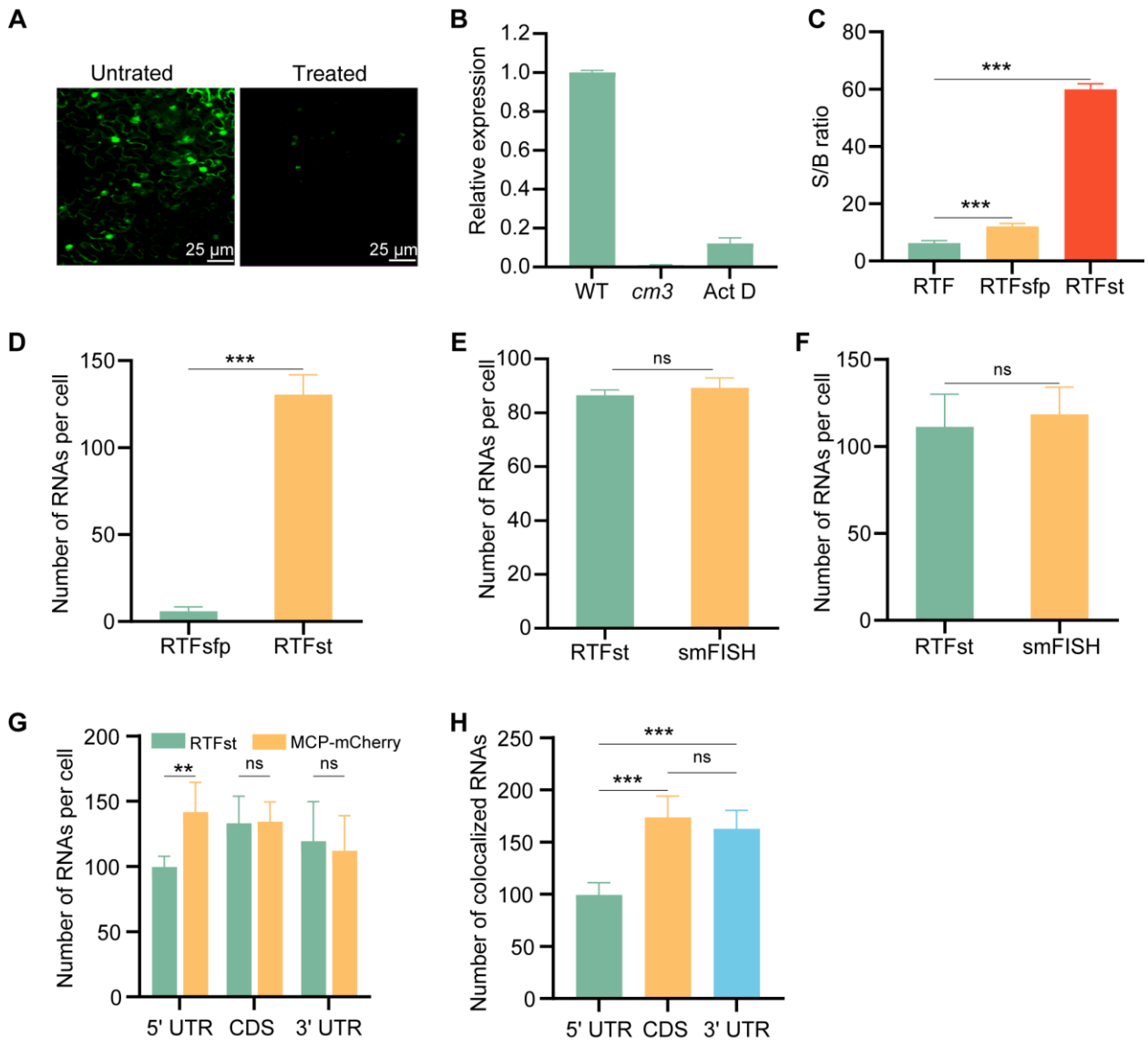

Fig. S3. Expression of RNA switch-controlled RTF system in plants.

(**A** and **B**) The RNA switch–RTF system exhibits a degree of leakage in the absence of the target RNA. (**A**) Fluorescence imaging of *N. benthamiana* leaf epidermal cells expressing the RNA switch–RTF system targeting *CM3* mRNA. 'Untreated' indicates cells not exposed to Actinomycin D (Act D), an RNA synthesis inhibitor, while 'treated' indicates cells subjected to 20 μM Act D treatment. Scale bars: 25 μm. (**B**) Relative expression levels of *CM3* mRNA in wild-type (WT), *cm3* mutant, and Act D-treated WT plants determined by qRT–PCR. (**C**) Quantification of the signal-to-noise ratio (SNR) for RTF, RTF–SFP, and RTF–SunTag in *cm3* mutants (n = 6, mean ± s.e., *** $P < 0.001$, one-way ANOVA with multiple comparisons and a post-hoc test). (**D**) The number of well-dispersed diffraction-limited fluorescent puncta per cell (n = 6, mean ± s.e.m.,

895 **** $P < 0.001$, two-tailed unpaired Student's t-test). **(E** and **F)** Quantification of *CM3* mRNA in
896 individual root (**E**) and leaf (**F**) cells using smFISH and RNA switch–RTFst. Statistical
897 comparisons for root cells (n = 6, mean ± s.e., $P > 0.05$, non-significant [ns], two-tailed unpaired
898 Student's t-test) and leaf cells (n = 6, mean ± s.e., $P > 0.05$, ns, two-tailed unpaired Student's t-
899 test). (**G**). Quantification of *CM3* mRNA detected by RNA switch–RTFst and mCherry–MCP–
900 MS2 (n = 6, mean ± s.e, ns, $P > 0.05$; $P < 0.01$, two-tailed unpaired Student's t-test). (**H**) Number
901 of colocalized *CM3* mRNAs detected by RNA switch–RTFst and mCherry–MCP–MS2 (n = 6,
902 mean ± s.e., ***$P < 0.001$, one-way ANOVA with multiple comparisons and a post-hoc test).
903

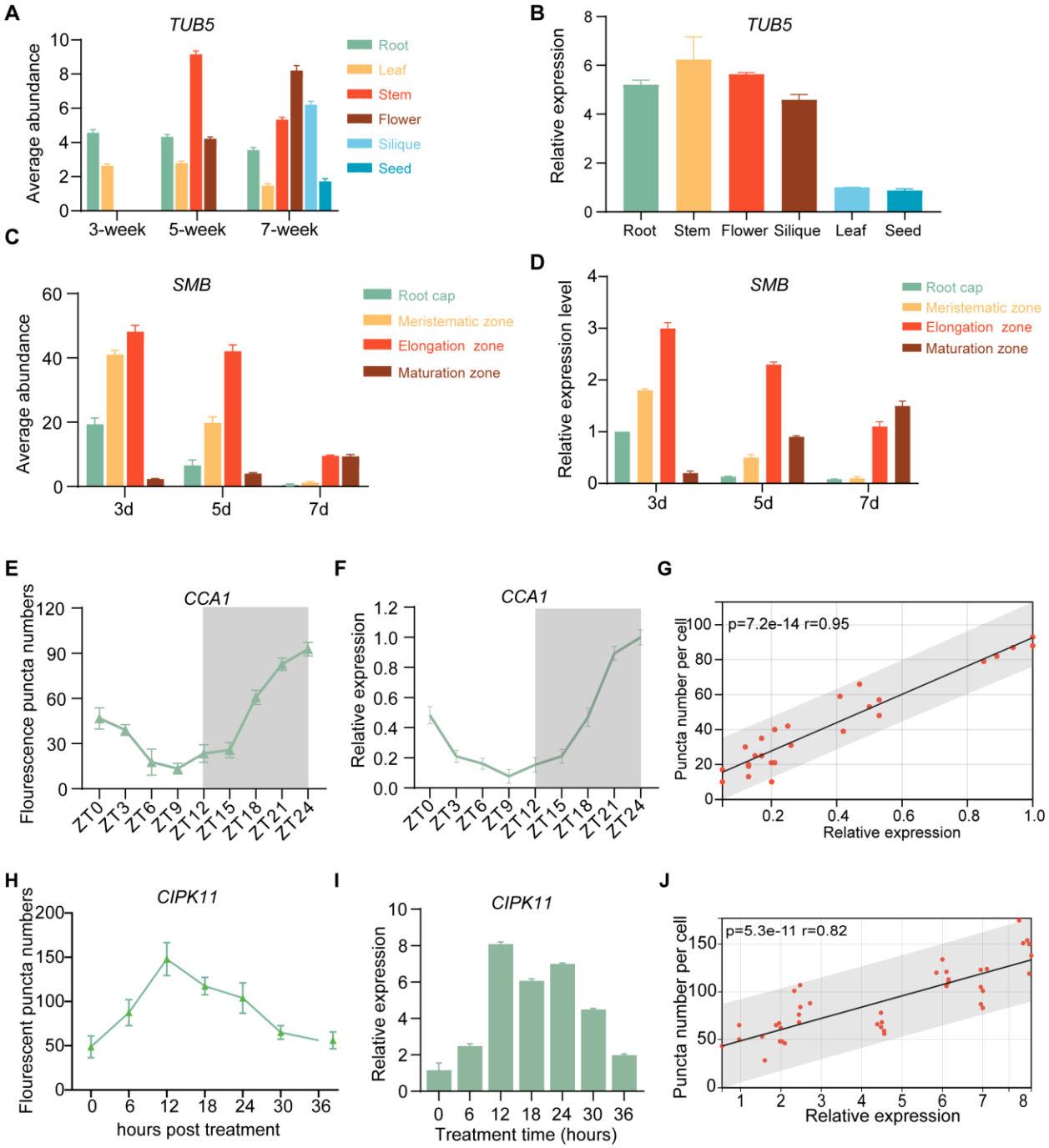

Fig. S4. Quantification of RNA abundance using RNA switch–RTFst in living plants. (**A**) Average abundance of *TUB5* in different tissues as measured by RNA switch–RTFst. (**B**) Relative expression levels of *TUB5* in different tissues of 7-week-old *A. thaliana* seedlings assessed by RT–qPCR. (**C**) Average abundance of *SMB* in root tip tissues, as revealed by RNA switch–RTFst. (**D**) Relative expression levels of *SMB* in root tip tissues assessed by RT–qPCR at 3, 5, and 7 d after germination. (**E** and **F**) Circadian patterns of *CCA1* expression in leaves of 7-

911 week-old *A. thaliana* depicted by RNA switch–RTFst quantification (**E**) and RT–qPCR (**F**). Light
912 phase began at Zeitgeber Time 0 (ZT0) and dark phase (shaded areas) began at ZT12. (**G**)
913 Correlation between *CCA1* expression levels measured by RNA switch–RTFst and RT–qPCR. (**H**
914 and **I**) Average abundance of *CIPK11* in roots of 7-week-old Arabidopsis under cadmium (Cd)
915 stress as determined by RNA switch–RTFst (**H**) and RT–qPCR (**I**). (**J**) Correlation between
916 *CIPK11* expression levels measured by RNA switch–RTFst and RT–qPCR.
917

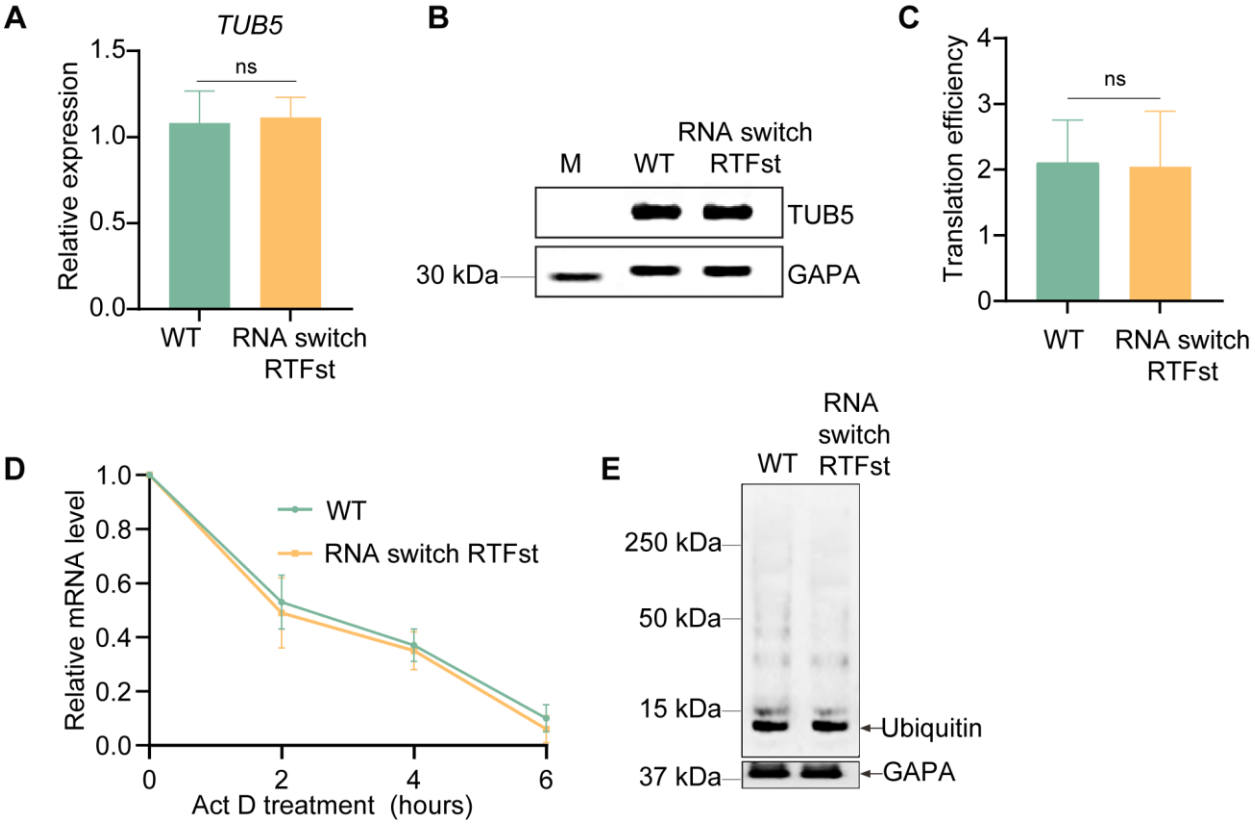

Fig. S5. The fate of *TUB5* mRNA in Arabidopsis thaliana is unaffected by the RNA switch-RTFst system.

(**A**) Relative expression levels of *TUB5* mRNA in WT plants and plants expressing RNA switch–RTFst (n = 9, mean ± s.e., ns, non-significant, $P > 0.05$, two-tailed unpaired Student's t-test). (**B**) Western blot of TUB5 abundance in WT plants and plants expressing RNA switch–RTFst. GLYCERALDEHYDE 3-PHOSPHATE DEHYDROGENASE A SUBUNIT (GAPA) was used as a loading control. (**C**) Translation efficiency of *TUB5* mRNA in WT plants and plants expressing RNA switch–RTFst calculated by normalizing TUB5 abundance to *TUB5* mRNA levels (n = 9, mean ± s.e., ns, non-significant, $P > 0.05$, two-tailed unpaired Student's t-test). (**D**) Degradation dynamics of *TUB5* transcripts following Act D treatment in the roots of WT and plants expressing RNA switch–RTFst. One-week-old *A. thaliana* seedlings were treated with 20 μM Act D, and relative *TUB5* transcript levels were quantified by RT–qPCR at 0, 2, 4, and 6 h post-treatment. (**E**) Western blot of the overall ubiquitinated protein in WT and switch–RTFst-expressing lines. GAPA was used as a loading control.

Table S1.

Twenty amino acids at the C-terminal of 17 proteins detected in MG132-treated *N. benthamiana* leaves. The reference proteins of *N. benthamiana* were download from Sol Genomics Network database (https://solgenomics.net/ftp/genomes/Nicotiana_benthamianaV261/Nbenthamiana_Annotation/)

Protein	C-terminal peptide (CP) name	Amino-acid sequence	Gene ID
Niben261Chr01g0596013.1	CP-1	WSSDHIALLAEFRCKPRTRR	107761103
Niben261Chr04g1859023.1	CP-2	NIFPLWGLAEYRKNVLLQNY	107770515
Niben261Chr06g0625009.1	CP-3	LDKPGFVPLLTAHMAGGLNV	107791570
Niben261Chr09g1100004.1	CP-4	KDGVHFHHFKDGKCSCCDFW	107760323
Niben261Chr10g0111025.1	CP-5	KWGCPVCRANIDQVIRLYAV	107777805
Niben261Chr12g0313004.1	CP-6	KLVYRFSSSSFGRAKNNDIP	107791192
Niben261Chr12g0827001.1	CP-7	FRDNDYIDILPKDIQPSRGT	107781174
Niben261Chr12g0990011.1	CP-8	TKVKQIYVAKQTISGTKTTG	107816357
Niben261Chr14g0257004.1	CP-9	LAGEAKMLCRDIAGHVEFFR	107827605
Niben261Chr14g1162005.1	CP-10	SRLVETGSSDQLDIGKPMIN	107782682
Niben261Chr17g0072018.1	CP-11	LLLKKFMKANGLGAVFMDES	107775987
Niben261Chr01g0008021.1	CP-12	ITGLLILFWRMQKRGRRRRG	107774733
Niben261Chr07g0989006.1	CP-13	MEGKFELWGLNYGLSHPHYV	107767796
Niben261Chr10g0130005.1	CP-14	GRVFVVVNWKLIVRDTPSMG	107761493
Niben261Chr04g0243021.1	CP-15	EKHFGLFSPDQRAKYQLNFN	107763289
Niben261Chr08g0313003.1	CP-16	LALTNQPFIVFFRKFQKTDG	107799889
Niben261Chr06g1467002.1	CP-17	LAEEAKTLAAALLEEEIMDN	107831752

Table S2.

Information on RNA-binding polypeptide (RBP) and RNA aptamers. Red font indicates shared amino-acid residues between ARM and RRRG degron.

Name	Sequences with degron (RRRG)	RBP	Sequence	RNA ligand	Reference
Rev–RRRG	TRQARRNRRRRWRE**RRRG**	HIV-1 Rev	TRQARRNRRRRWRERQR	RRE	(*8*)
P22N–RRRG	NAKTRRHERRRKLAIE**RRRG**	P22N	NAKTRRHERRRKLAIER	P22 boxB	(*9*)
λN–RRRG	MDAQTRRRE**RRRG**	λN	MDAQTRRRERRAEKQAQWKAAN	boxB	(*10*)
BTat–RRRG	SGRSRRSRGTRGKGRRIR**RRG**	BIV-Tat	SGRSRRSRGTRGKGRRIRR	Pepper	(*11*)
HTat–RRRG	SYGRKKRRQ**RRRG**	HIV-Tat	SYGRKKRRQRRRRSRSQ	HIV-1 TAR	(*12*)
Rex–RRRG	MPKTRRRPRRSQRK**RRRG**	HTLV-1 Rex	MPKTRRRPRRSQRKRP	XBE	(*13*)

Table S3.

RNA switches for imaging *mCherry* RNA. The red, brown, black and blue font indicates respectively the RRE aptamer, linker 1, the probe sequence, and linker 2 in RNA switches.

Target site	RNA switch (RS) name	Sequence
AGCAAGGGCGAGGAGGAUAACA	RS#1	GGUCUGGGCGCAGCGCAAGCUGACGGUACAGGCCAGUGUUAUCCUCCUCGCCCUUGCUGG
	RS#2	GGUCUGGGCGCAGCGCAAGCUGACGGUACAGGCCAGCAUGUUAUCCUCCUCGCCCUUGCUGGCC
	RS#3	GGUCUGGGCGCAGCGCAAGCUGACGGUACAGGCCAGCAAGUGUUAUCCUCCUCGCCCUUGCUGGCCUG
UGGCCAUCAUCAAGGAGUUCAU	RS#4	GGUCUGGGCGCAGCGCAAGCUGACGGUACAGGCCGTGCAGGGGGCCACCCUUGGUCACGG
	RS#5	GGUCUGGGCGCAGCGCAAGCUGACGGUACAGGCCGUGAGCAGGGGGCCACCCUUGGUCACGGCC
	RS#6	GGUCUGGGCGCAGCGCAAGCUGACGGUACAGGCCGUGACCGCAGGGGGCCACCCUUGGUCACGGCCUG
UUCAAGUGGGAGCGCGUGAUG	RS#7	GGUCUGGGCGCAGCGCAAGCUGACGGUACAGGCCCUCAUCACGCGCUCCCACUUGAAGGG
	RS#8	GGUCUGGGCGCAGCGCAAGCUGACGGUACAGGCCCUUCCAUCACGCGCUCCCACUUGAAGGGCC
	RS#9	GGUCUGGGCGCAGCGCAAGCUGACGGUACAGGCCCUUCAACAUCACGCGCUCCCACUUGAAGGGCCUG
UCGUUGUGGGAGGUGAUGUCCA	RS#10	GGUCUGGGCGCAGCGCAAGCUGACGGUACAGGCCUGUCGUUGUGGGAGGUGAUGUCCAGG
	RS#11	GGUCUGGGCGCAGCGCAAGCUGACGGUACAGGCCUGGAUCGUUGUGGGAGGUGAUGUCCAGGCC
	RS#12	GGUCUGGGCGCAGCGCAAGCUGACGGUACAGGCCUGGACAUCGUUGUGGGAGGUGAUGUCCAGGCCUG

Table S4.

smFISH probes used for targeting *CM3* mRNA.

Probe	Sequence (5′ – 3′)	5′ labeling
Probe 1	aacgcgggtttgagtaacttag	Cy3
Probe 2	aatcgcgagatgagtcttgaag	Cy3
Probe 3	aggaagagagacccagaagata	Cy3
Probe 4	aaatactcactctcatctaccc	Cy3
Probe 5	aagataatactgtcctcttgac	Cy3
Probe 6	aagataatactgtcctcttgac	Cy3
Probe 7	tttcagtttctctgaccataaa	Cy3
Probe 8	taggaggaaggataggttcagg	Cy3
Probe 9	taggaggaaggataggttcagg	Cy3
Probe 10	ctgaaccacaattaccgtcatc	Cy3

Table S5.

Specific probe sequences targeting the 5' UTR, coding sequence and 3' UTR of *CM3* mRNA.

Probes	**Sequence (5′ – 3′)**
$P_{5' UTR}$	AGAGACAGAGACAGAGAGTGGA
P_{CDS}	CAAATACTCACTCTCATCTACC
$P_{3' UTR}$	AAATGTTATGCTTCCTTCTTTG

Table S6.

Identifiers for Arabidopsis target genes.

Gene name	Locus	Gene ID
TUB5	AT1G20010	838590
CCA1	AT2G46830	819296
CIPK11	AT2G30360	817586
SMB	AT1G79580	844296

Table S7.

Primers for genotyping of Arabidopsis mutants and RT–qPCR.

Purpose	Gene	Forward primer	Reverse primer	T-DNA left-border primer
Genotyping identification	*cm3*	LP: TGTGGGGTCAGGAATTTAATG	RP: AAGAAAAGGACAGAGGAACGG	LB: ATTTTGCCGATTTCGGAAC
	tctp1	CAAGCAAGATACGATAGATTGGGGT	TAACCTTTCAGGATCAGGCTGAGG	ATAATAACGCTGCGGACATCTACATTTT
RT–qPCR	*CM3*	TCCCCAAACCTCAATCTTAC	ACTCACTCTCATCTACCCTT	
	CIPK11	CAGATCAAGTTCCACGATGA	CCCGACGAGTAAGAAATCAA	
	CCA1	AAGGTGGACTGAGGAAGAACATA	AGCCTCTTTCTCTACCTTGGA	
	TCTP1	AAGGAAAGTGGGTTACTGTG	TAAGTTGGTTGCTCCTGAAG	
	VDAC3	TTCACGACCAAAGAGAACG	TGAAGAACGACTTTGGACG	
	Ya1	ACAAGTCCAATCTGCCAAG	ACTGATTTATTTTGCGGTGG	
	SMB	GTCCTCAAAACGAGTGGTAT	CTTCTTGGAGCTGTTGAGAT	
	TUB5	TCGTCTTACTTCGTTGAGTG	TCCATTCCTTCTCCTGTGTA	

Table S8.

DNA sequences for *in vitro* transcription of RNA aptamers. Lowercase letters indicate the reverse complementary sequence of the *T7* promoter.

RNA aptamer	**DNA sequences of RNA aptamer**	**Reverse complementary sequence for *in vitro* transcription**
RRE	GGCTCGTGTAGCTCATTAGCTCCGAGCC	GGCTCGGAGCTAATGAGCTACACGAGCCcctatagtgagtcgtatta
P22 boxB	GGTGCGCTGACAAAGCGCGCC	GGCGCGCTTTGTCAGCGCACCcctatagtgagtcgtatta
boxB	GGGCCTGAAGAAGGGCCC	GGGCCCTTCTTCAGGCCCcctatagtgagtcgtatta
BIV TAR	GGCTCGTGTAGCTCATTAGCTCCGAGCC	GGCTCGGAGCTAATGAGCTACACGAGCCcctatagtgagtcgtatta
HIV-1 TAR	CCAGATCTGAGCCTGGGAGCTCTCTGG	CCAGAGAGCTCCCAGGCTCAGATCTGGcctatagtgagtcgtatta
XBE	GCTCAGGTCGAGGTACGCAAGTACCTCCCTTGGAGC	GCTCCAAGGGAGGTACTTGCGTACCTCGACCTGAGCcctatagtgagtcgtatta

Table S9.

Probe sequences in RNA switch for imaging target gene expression.

Gene	Probe sequence
SMB	ATTCTGCATTTCTCTTTAAGTT
CCA1	GGGAGGCCAAAATGATGAGGCG
CIPK11	CTCTTCCTCCTTCTTCTTCTTC
TCTP1	TAATGTAAGCGATGAATCCCTT
Ya1	CGGACTCCTTTATATACACT

Table S10.

Plasmids used in this study.

Type	Plasmid name	Purpose
RNA switch–RTF	pcambia1300-Ubq10-RTF	Expressing RTF
	pcambia1300-RSmCherry-RTF	Imaging mCherry RNA using RNA switch and RTF
	pcambia1300-RSCM3-RTF	Imaging CM3 RNA using RNA switch and RTF
RNA switch–RTF–SFP	pcambia1300-24XGFP11	Expressing 24XGFP11
	pcambia1300-RSCM3-GFP1-10	Expressing RSCM3 and GFP1-10
RNA switch–RTFst	pcambia1300-RSVDAC3-RTFst	Imaging VDAC3 RNA using RNA switch and RTFst
	pcambia1300-RSTUB5-RTFst	Imaging TUB5 RNA using RNA switch and RTFst
	pcambia1300-RSCM3-RTFst	Imaging CM3 RNA using RNA switch and RTFst
	pcambia1300-RSCIPK11-RTFst	Imaging CIPK11 RNA using RNA switch and RTFst
	pcambia1300-RSCCA1-RTFst	Imaging CCA1 RNA using RNA switch and RTFst
	pcambia1300-RSTCTP1-RTFst	Imaging TCTP1 RNA using RNA switch and RTFst
	pcambia1300-RSVDAC3-RTFst	Imaging VDAC3 RNA using RNA switch and RTFst
	pcambia1300-RSYa1-RTFst	Imaging RSYa1 RNA using RNA switch and RTFst
SM2–MCP	pcambia1300-24×MS2	Expressing 24×MS2
	pcambia1300-mCherry-MCP	Expressing mCherry-MCP

Video S1.

Cell-to-cell trafficking of *TCTP1* mRNA in Arabidopsis root.

Video S2.

Visualization of aphid-secreted *Ya1* in *N. benthamiana* leaves.

References

1. V. Demichev, C. B. Messner, S. I. Vernardis, K. S. Lilley, M. Ralser, DIA-NN: neural networks and interference correction enable deep proteome coverage in high throughput. *Nat. Methods* **17**, 41-44 (2020).
2. S. J. Harrison *et al.*, A rapid and robust method of identifying transformed seedlings following floral dip transformation. *Plant Methods* **2**, 1-7 (2006).
3. N. Tsanov *et al.*, smiFISH and FISH-quant - a flexible single RNA detection approach with super-resolution capability. *Nucleic Acids Res.* **44**, 1-11 (2016).
4. M. Michaud *et al.*, Differential targeting of VDAC3 mRNA isoforms influences mitochondria morphology. *P. Natl. Acad. Sci. USA* **111**, 8991-8996 (2014).
5. C. Y. Li *et al.*, Rice stripe virus activates the bZIP17/28 branch of the unfolded protein response signalling pathway to promote viral infection. *Mol. Plant Pathol.* **23**, 447-458 (2022).
6. Z. Yang *et al.*, RNase H1 Cooperates with DNA Gyrases to Restrict R-Loops and Maintain Genome Integrity in Arabidopsis Chloroplasts. *Plant Cell* **29**, 2478-2497 (2017).
7. Y. S. Lai *et al.*, Systemic signaling contributes to the unfolded protein response of the plant endoplasmic reticulum. *Nat. Commun.* **9**, 1-11 (2018).
8. J. L. Battiste et al., Alpha helix-RNA major groove recognition in an HIV-1 Rev peptide-RRE RNA complex. *Science* **273**, 1547-1551 (1996).
9. R. J. Austin, T. Xia, J. Ren, T. T. Takahashi, R. W. Roberts, Designed arginine-rich RNA-binding peptides with picomolar affinity. *J. Am. Chem. Soc.* **124**, 10966-10967 (2002).
10. P. Legault, J. Li, J. Mogridge, L. E. Kay, J. Greenblatt, NMR Structure of the Bacteriophage λ N Peptide/boxB RNA Complex: Recognition of a GNRA Fold by an Arginine-Rich Motif. *Cell* **93**, 289-299 (1998).
11. J. D. Puglisi, L. Chen, S. Blanchard, A. D. Frankel, Solution Structure of a Bovine Immunodeficiency Virus Tat-TAR Peptide-RNA Complex. *Science* **270**, 1200-1203 (1995).
12. C. A. Smith, V. Calabro, A. D. Frankel, An RNA-Binding Chameleon. *Mol. Cell* **6**, 1067-1076 (2000).
13. F. Jiang et al., Anchoring an extended HTLV-1 Rex peptide within an RNA major groove containing junctional base triples. *Struct. Fold. Des.* **7**, 1461-1472 (1999).